FIRST PRINCIPLE MODELING OF HYBRID HALIDE PEROVSKITES FOR OPTOELECTRONIC APPLICATIONS

by

Eric William Welch, M.S.

A dissertation submitted to the Graduate Council of
Texas State University in partial fulfillment
of the requirements for the degree of
Doctor of Philosophy
with a Major in Material Science, Engineering and Commercialization
December 2019

Committee Members:

Alexander Zakhidov, Chair

Luisa Scolfaro

Todd Hudnall

Shane Yost

Amanda Neukirch

FAIR USE AND AUTHOR'S PERMISSION STATEMENT

Fair Use

Duplication Permission

DEDICATION

This dissertation is dedicated to my mother, Rosemary Welch (02/01/1959 – 07/31/2008). Your love and compassion live on inside me and drive me to be the best I can be. I miss you.

ACKNOWLEDGEMENTS

First, I'd like to thank Dr. Alex Zakhidov for his immense support and patience through my growth as a scientist. As the lone theorist in his group, I appreciate his knowledge and guidance in gaining intuition for both experimentation and computation. I thank him for opening doors to incredible opportunities like working at Los Alamos National Lab and traveling to national conferences to share our work and results.

Second, I'd like to thank Dr. Luisa Scolfaro for her knowledge and help in my growth as a theorist employing density functional theory to study optoelectronic materials. Her guidance and help in contacting me with experts inspired me to study the mathematical framework of material modeling.

Both Dr. Zakhidov and Dr. Scolfaro introduced me to chemists who are experts in both optoelectronic experimentation and theory at Texas State in Dr. Todd Hudnall and Dr. Shane Yost, respectively. I greatly appreciate both of their inputs for my understanding of the chemical nature of the physical processes of which I have been studying. Their insight and understanding of semiconducting materials and quantum chemistry modeling helped me to better understand all aspects of how materials are studied.

I'd like to thank Dr. Amanda Neukirch for helping while I was a visiting student user at the Center for Integrated Nanotechnology (CINT) at Los Alamos National Lab. She also helped me understand different photophysical processes in perovskite materials.

Next, I'd like to thank my father for his support and love throughout my life. His selflessness and perseverance during my childhood has always been a guiding light for me. I really appreciate everything he's done for me through my life.

And last, I'd like to thank the love of my life Gabby Harmon. Her patience and support both as a partner and peer kept me sane and grounded through many chaotic times throughout my PhD. She was and continues to be the rock upon which I find solace and strength. I appreciate her beyond measure. *Love you girlfriend.*

TABLE OF CONTENTS

Page

LIST OF TABLES

Table **Page**

LIST OF FIGURES

Figure **Page**

LIST OF ABBREVIATIONS

Abbreviation	Description
HP	Halide Perovskite
OE	Optoelectronic
PV	Photovoltaics
LED	Light Emitting Diode
DSSC	Dye Sensitized Solar Cell
IHP	Inorganic Halide Perovskite
HHP	Hybrid Halide Perovskite
MA	Methylammonium
FA	Formamadinium
DFT	Density Functional Theory
LDA	Local Density Approximation
PBE	Perdew-Berke-Ernzerhof
LSDA	Local Spin Density Approximation
VASP	Vienna Ab-Initio Simulation Package
GGA	Generalized Gradient Approximation
HSE	Heyd-Scuseria-Ernzerhof
PAW	Projector Augmented Wave

RMM-DIIS	Residual Minimization Scheme with Direct Inversion in the Iterative Subspace
VBM	Valence Band Maximum
CBM	Conduction Band Minimum
DOS	Density of States
GW	Green's Functions
VESTA	Visualization for Electronic and Structural Analysis
SCF	Self-Consistent Field
SOC	Spin Orbit Coupling
CPGE	Circular Photogalvanic Effect
CAGR	Compound Annual Growth Rate
PVP	Perovskite Photovoltaic
USD	United States Dollar
BPVE	Bulk Photovoltaic Effect
LPGE	Linear Photogalvanic Effect
PCE	Power Conversion Efficiency
ITO	Indium Tin Oxide
CW	Continuous Wave

ABSTRACT

Halide perovskites (HP) are a promising material for use in solar cells and electronic devices, offering a comparable, less expensive alternative to current technologies. Devices with impressive optical and electronic properties are being made in the lab, but a robust theoretical understanding on the underlying photophysics in HPs is required to improve current devices and predict future devices. The causes for positive device behaviors like long charge carrier lifetimes and long diffusion lengths, and high carrier mobility as well as detrimental device behavior like degradation and instability are both topics of debate and may be studied from first principle using modern, state-of-the-art computational software and high-power computing clusters. In this work, HP materials are studied using ab-initio methods to study the ground state and excited state properties. A model used in oxide perovskites is shown to work well in HPs to model polaronic properties, as these materials exhibit ionic bonding and therefore are predicted to exhibit strong electron-phonon coupling. Relativistic effects are studied using spin orbit coupling (SOC) corrections to account for large atoms like Pb and I. The Rashba effect is seen when SOC corrections are added which implies inversion symmetry breaking and momentum dependent photoexcitation, both of which were confirmed in experiments done by our collaborators. The strength and effect of SOC on mixed metal and mixed halide perovskites shows that the benchmark HP $CH_3NH_3PbI_3$ (MAPI) has the largest splitting, indicating promising potential for applications in ultrafast optical detectors, while other mixed HPs may be used as spin-injection and transport materials.

Finally, the band offset method for studying interfaces revealed the lowest energy face between the HP $CsPbBr_3$ and CuI to be the $PbBr_2$ on Cu interface, where a type II band offset indicates charge separation at the interface; CuI is predicted to be a viable, low cost, alternative charge transport material for HP devices. HPs have already excited the solar cell community with the promise of affordable alternatives that will be cheaper than the current fossil fuels causing anthropogenic climate change and have the chance to create the same fervor in other semiconductor arenas as research continues to improve our understanding.

1. INTRODUCTION

Halide perovskites (HP) are a class of semiconducting material that have revolutionized the field of optoelectronics (OE) over the last decade. HPs are comprised of earth-abundant elements[1] like C, N, H, Pb, Br and I that are combined to form inexpensive precursors e.g. CH_3NH_3I and PbI_2 which are solution-processed at room temperature to create OE devices; room-temperature processing opens the door for direct deposition onto flexible substrates, a near requirement for modern commercial applications. HP materials truly emerged through the field of photovoltaics (PV), where device efficiency improved rapidly from 3% to over 25%[2] in less than 10 years of research, as shown in fig 1; for reference, similar two-junction Si-based solar cells in the market have 35.5% which took over 35 years of research and are still very expensive to produce. HPs have subsequently been used in other optoelectronic devices like light emitting diodes (LEDs)[3,4,5], lasers[6,7], photodetectors[8] and even exotic applications like light emitting field effect transistors[9,10].

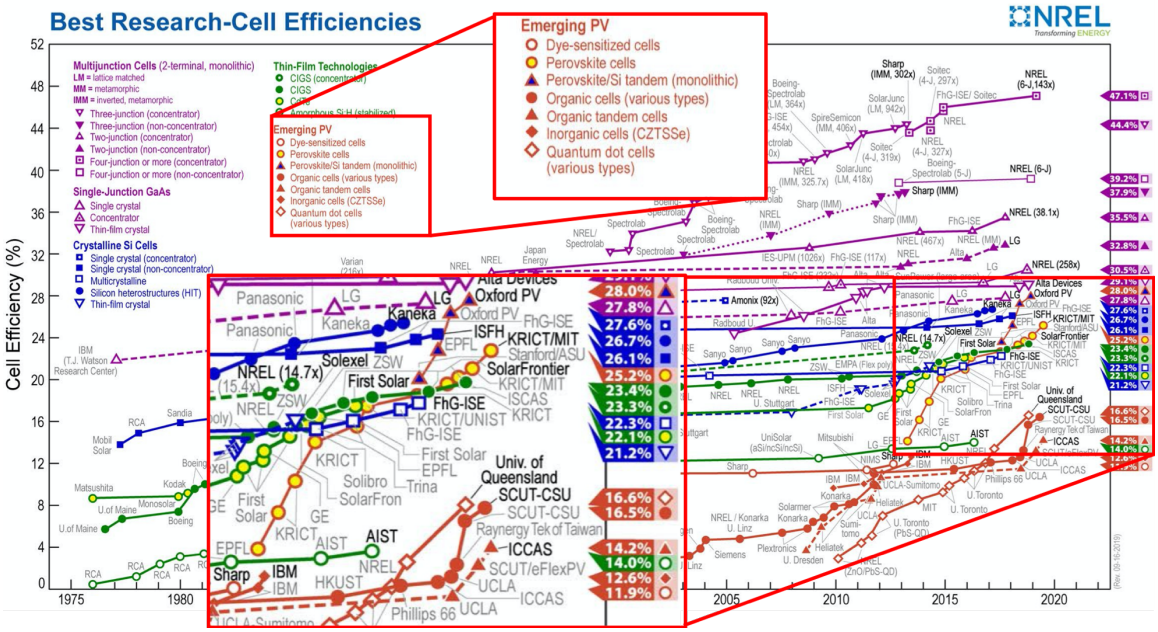

Figure 1. NREL solar cell efficiency chart, taken from August 2019. Regions detailing perovskite solar cells are highlighted and enlarged.

The application of HPs in modern optoelectronic devices has resulted in marked improvements in device performance as well as offering an inexpensive alternative to traditional semiconducting materials. HP materials result in devices with favorable OE characteristics which require understanding through both first-principle modeling/calculations and experimentation. This manuscript aims to tackle the former through density functional theory calculations which highlight the ability to tune different device properties through atomistic/stoichiometric mixing.

Perovskite is the term given to the family of compounds that form the ABX_3 structure. This crystal structure was discovered inside a meteorite containing $CaTiO_3$ (calcium titanate) in the Ural Mountains by chemist Gustav Rose in the early 20th century and named for the Russian mineralogist Count Lev Alekseyevich von Perovski[11]. 10 years after the discovery, H. L. Wells[12] synthesized the first perovskite materials which

showed photoconductivity during experiments by C. K. Møller[13]. Oxide perovskites were the first family of perovskite materials used and studied in the 1950s for a variety of applications such as fuel cells, condensers, electromechanical transducers, catalysts, gas sensors, heating elements, lasers, superconducting devices and multilayer capacitors[14]. It took a further 50 years of research before perovskites would be used as the absorbing layers in solar cells, first as an electrolyte-buffer layer in dye sensitized solar cells (DSSC) and then as the complete active layer once it was realized that perovskites alone were far more efficient than DSSCs. The first device created by M. Chikao et al. used rare earth materials to create an oxide perovskite solar cell, but it was later realized that earth-abundant materials can be used to create HPs which resulted in efficient solar cells[14]. Over the last decade of research, HP solar cells have increased their efficiency and the perovskite research community has helped to elucidate photophysical mechanisms behind many of the remarkable device properties seen in lab.

Figure 2. shows the typical perovskite structure. Two sublattices interlock to form the structure: (1) A large cation resides in the A-site (red atom) octahedral vacancy with 12-fold coordination, (2) surrounded by a BX_6 cage (green and blue atoms). The importance of distinguishing between these two sublattices lies in the fact that the valence edge states of HPs are predominantly comprised of X p-orbitals and the conduction edge states are predominantly comprised of B p-orbitals. This implies that photophysical processes occur almost entirely within the B-X framework of the perovskite while, unless the A-site is comprised of an organic molecular dipole, the A framework is mostly inert; if the A-site is an organic dipole, rotational dynamics might influence charge carrier motion. In this manuscript, the two main classes of perovskite

are defined by the choice of the A-site cation: (1) inorganic halide perovskites (IHP) contain a single element at the A-site e.g. Cs or Ca, or (2) hybrid halide perovskites (HHP), which contain an organic molecule like methylammonium (CH_3NH_3) at the A-site.

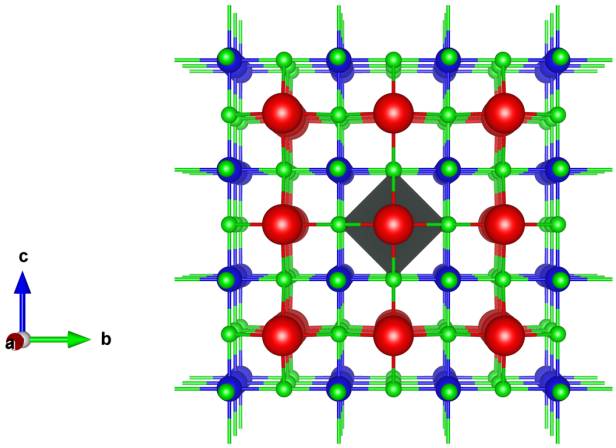

Figure 2. ABX_3 Perovskite structure with A (red), B (blue) and X (green) atoms shown in a perspective view. A single octahedron is superimposed around the central A-site atom to show symmetry and coordination.

Atomic size and charge neutrality are two initial factors which help to predict whether a compound forms the perovskite structure. The Goldschmidt tolerance factor, given by $t = \frac{r_A + r_X}{\sqrt{2}(r_B + r_X)}$ where r_A, r_B, and r_X are the atomic radius of each atom, is an initial metric by which a compound may be predicted to form the perovskite structure[15]; a stable perovskite structure has a tolerance factor of $t = 1 \pm 0.2$. This implies that not all compounds will form the perovskite structure. The tolerance factor, however, is not enough by itself to predict the perovskite structure. Charge neutrality coupled with the Goldschmidt factor, however, improves the approximation to find perovskite compounds, where ABX_3 charge balancing is ensured when $q_{tot} = q^A + q^B + 3q^X = 0$, where q^A, q^B,

and q^X are the charge of each atom. While chalcogenides, specifically oxides, have multiple compounds which satisfy both the tolerance factor and charge neutrality[16], as $q^X = q^O = -2$ means $q_{tot} = 6$, halides are more restrictive with $q_{tot} = 3$; this is satisfied for I-II-X_3 compounds as well as HHPs with large enough organic molecules e.g. $CH_3NH_3^+$ (MA). IHPs and HHPs exist with halide anions utilizing I, Br and/or Cu, often in some stoichiometric mixture to take advantage of the tunability of HP's electronic properties. Also, HHPs often mix A-site cations with inorganic cations like Cs and organic cations like MA and formamadinium (FA) to similarly exploit the ability to tune device properties by mixing different cations. Sn is sometimes mixed with Pb in HHPs but is done more out of the misconception that Pb is harmful or toxic in these materials with the aim to remove the Pb altogether. To quell that fear, the author reminds readers that the amount of Pb is non-toxic and encapsulated within the solar cell device. Pb is only toxic if consumed in quantity and, as these devices are not meant to be consumed, the Pb content is inconsequential. However, the perovskite structure is still formed with Sn only or Sn mixed HPs and favorable device properties may be found in the future by replacing Pb completely in HPs.

The perovskite structure shows three main temperature dependent phase changes from the low temperature orthorhombic phase to the intermediate temperature tetragonal phase to the high temperature cubic phase; other phases exist but are due to structural changes like lowering of the dimensionality of the material. Time-resolved x-ray diffraction measurements reveal a direct, reversible transition from the orthorhombic to cubic phase near 400 K in IHPs[17], while temperature-dependent photoluminescence measurements reveal HHPs have all three main phase changes with the orthorhombic to

tetragonal phase change occurring near 160 K and the tetragonal to cubic phase change occurring near 310 K[18]; IHPs may also exist in the tetragonal phase, but favor the direct orthorhombic to cubic transition due to the lack of rotational freedom in the A-site.

As a semiconducting material, HPs are considered intrinsic semiconductors with no currently known way to dope the material. This implies multiple things when HPs are used as an active layer material in optoelectronic devices. In absorbing applications like solar cells or photodetectors, HPs form mobile charge carriers upon photoexcitation but are unable to move the charges without transport layers placed on either side of the HP material, resulting in rapid radiative recombination which is unwanted. Thus, transport materials are chosen to move electrons and holes away from the HP material to harvest the photoexcited electrons as a photocurrent. In emitting applications like lasers and LEDs, the HP's attractive optoelectronic properties like a small, direct band gap allow for efficient charge accumulation and recombination within the HP material. Again, transport layers are used with these HP devices to move electrons and holes into (instead of out of) the HP material, increasing the likelihood of radiative recombination with electrons and holes excited due to an applied voltage bias. With the transport layers, using the nomenclature of semiconducting devices, HP devices form a p-i-n junction device, where p-i-n represents p-type, intrinsic, and n-type semiconducting layers, respectively; fig 3 shows a toy model of a p-i-n junction device.

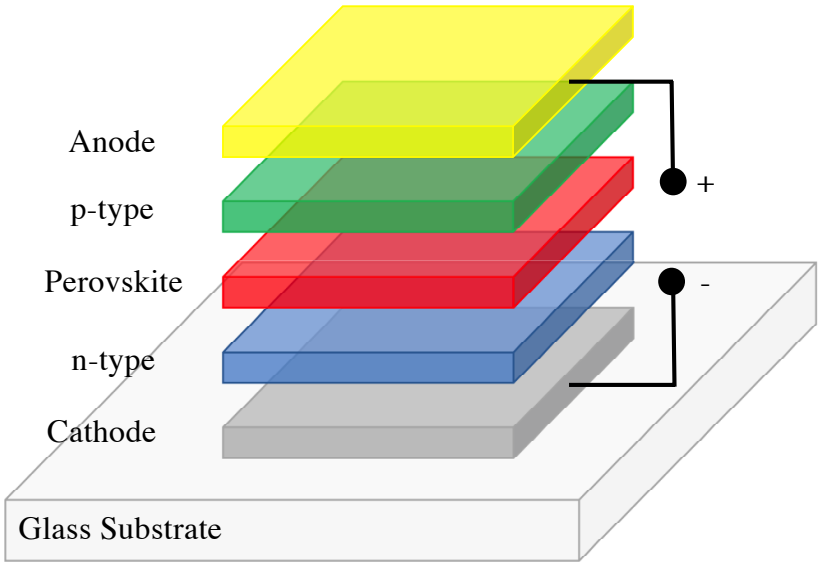

Figure 3. Toy model of an HP solar cell device stack atop a glass substrate.

This work has numerous motivations for each step in understanding the photophysical processes in HPs. Crystal structure optimization is the first step of every material computational study and the initial structures are taken from the ever growing Materials Project[19] and are individually optimized. P. Erhart's work on modeling polarons in oxide perovskites is the basis for the polaron study in HPs in this work[20]; this work shows that the method used to reveal polarons in oxide perovskites also successfully reveals polarons in HPs. Also, the computational approximations used for oxides is also shown to successfully model HPs. Next, the effects of atomic size are studied to show how larger atoms exhibit relativistic behavior and give rise to Rashba splitting when the system has broken inversion symmetry. These effects were studied for mixed HP materials, and confirmed experimentally for benchmark HP solar cells by colleagues using THz emission spectroscopy, results which will be detailed later in this

manuscript. Relativistic effects are further studied for mixed HPs to show the trends in electronic properties with the aim to predict possible spintronic applications. Next, the interface between an IHP and an inorganic semi-conducting charge transport material is studied to elucidate transport properties for light emitting applications. Finally, a summary perspective on charge carrier dynamics and polaron behavior in HPs is given.

This manuscript is thus broken into five parts. Part I is an introduction to the history of perovskites and perovskite-based devices as well as the motivations for this work. Part II details the theoretical and computational background of the methods used to study HP optoelectronic properties. Part III gives results and discussion of calculations studying the photophysical properties of HPs as well as HP-inorganic semiconductor (e.g. CuI) interfaces. Part IV is a summary of the current global and US markets for the two main industries in which HPs will initially emerge i.e. solar and LEDs, for both total market and then predicted perovskite market. Part V concludes this work and outlines potential future work.

2. THEORETICAL AND COMPUTATIONAL BACKGROUND

2.1. Historical Perspective

The foundation of modern material modeling is density functional theory (DFT), a mathematical model for simplifying and solving the many-body, many-interaction Schrödinger equation. The history of landmark breakthroughs in material modeling and DFT are summarized well by F. Giustino[21] and will be briefly summarized in the following section, highlighting papers which affect the current work.

History of DFT:

The seminal paper by Hohenberg and Kohn in 1964 forms the foundation for DFT. DFT is a theory which postulates that the ground state energy of an interacting system of atoms is a functional of the system's density which is a simple function of the position. It was shown that there exists a general functional of the density that correctly determines the ground state of each system and is independent of any external potentials; minimization of this functional would be all that was required to determine the ground state[22]. It is now well known that no exact functional exists due to the difficulty in accurately modeling electronic exchange and correlation. The term functional is defined as a function of a function; in other words, where a function takes a number as its argument and returns a number, a functional takes a function as its arguments and returns a number. For instance, a definite integral for a general integrand is a functional of the integrand such as $F[f(x)] = \int_0^1 f(x)dx$ where, if $f(x) = x^2$, then $F[f(x)] = \int_0^1 x^2 dx = \frac{1}{2}$.

Magnetic materials and relativistic effects were added to density functional theory by von Barth and Hedin in 1972 and Rajagopal and Callaway in 1973; spin was included through the generalization of quantum electrodynamics to DFT[23,24].

Starting in the 1980s, multiple groups began working on what is still, to this day, the most challenging issue facing DFT: electronic exchange and correlation, the effects of what happens when two electrons' positions are exchanged and the effective distance over which the charge of each electron is felt, respectively. The exchange and correlation are treated with a potential energy term in the Hamiltonian called the exchange-correlation functional. Ceperley and Alder in 1980 and Perdew and Zunger in 1981 developed the local density approximation to the electronic exchange and correlation functionals. This approximation solves the equations of DFT only at a single site while averaging over the rest of the sites; this method is done iteratively for each site, updating the total potential with each previous local potential. Quantum Monte Carlo calculations were used with the local density approximation to determine the exchange-correlation energy of the uniform electron gas; these results are considered the emerging point where DFT could be used to model real materials[25,26].

Pseudopotential theory was developed in the nineteen fifties and sixties where it was realized that nuclear core potentials could be approximated with a 'pseudo' potential, and only valence electron were included in DFT calculations. The Born-Oppenheimer approximation was utilized to separate the motion of the ionic core and the fast-moving electrons whose mass is several orders of magnitude smaller than the ionic core, and thus, move orders of magnitude more quickly. Therefore, the solution to the partial differential equations of DFT may be approximated as a product solution of a purely electronic and

purely ionic component. The ionic component is then considered an average over all ionic cores resulting in the pseudopotentials used in DFT calculations.

More advances in the 1980s occurred, as computational power became more accessible, with Runge and Gross developing the time dependent DFT formalism[27], Car and Parrinello developing molecular dynamics in DFT[28], and Baroni, Giannozzi and Testa implementing perturbation theory into DFT[29]. Then, in the 1990s, the entire periodic table was opened to being studied using DFT with the implementation of Hubbard-like corrections, where d- and f-orbitals could now be modeled[30,31]. Since the early 2000s, efforts in advancing DFT calculations have focused heavily on increasing the level of theory in treating electronic exchange and correlation, with local density approximation (LDA) and semi-local Perdew-Berke-Ernzerhof (PBE)[32] functionals being replaced or modified by non-local, range-separated, hybrid functionals which include portions of the exact Hartree-Fock exchange along with semi-local correlation; the level of theory one uses is usually dictated by the amount of computational power available for calculations.

2.2. Quantum Mechanics Background

As stated above, DFT, at its core, is an elegant method for solving the many-body Schrödinger equation. The single-particle Schrödinger equation is given by (in Dirac notation),

$$(\frac{\boldsymbol{p}^2}{2m} + V)|\Psi\rangle = E|\Psi\rangle, \quad (1)$$

where $\boldsymbol{p} = -i\hbar\boldsymbol{\nabla}$, V is the collection of potential energy terms, and Ψ and E are the eigenvector and eigenvalue of the Hamiltonian operator, respectively. The full many-body, many-interaction equation is given by,

$$\left[-\sum_i \frac{\hbar^2}{2m_e}\nabla_i^2 - \sum_I \frac{\hbar^2}{2m_N}\nabla_I^2 + \frac{1}{2}\sum_{i\neq j}\frac{e^2}{4\pi\epsilon_0}\frac{1}{|\boldsymbol{r_i}-\boldsymbol{r_j}|} + \frac{1}{2}\sum_{I\neq J}\frac{e^2}{4\pi\epsilon_0}\frac{Z_I Z_J}{|\boldsymbol{R_I}-\boldsymbol{R_J}|} - \sum_{i,I}\frac{e^2}{4\pi\epsilon_0}\frac{Z_I}{|\boldsymbol{r_i}-\boldsymbol{R_I}|}\right]\Psi = E_{tot}\Psi, \quad (2)$$

where the sums over i are for electrons while the sums over I are for nuclei. $\hbar$ is Planck's reduced constant, m_e is the electron mass, m_N is the nuclear mass, e is the electron charge, r_i (r_I) is the position of the *ith (Ith)* electron (nucleus), Z_I is the charge of the *Ith* nucleus, and E_{tot} and Ψ are the eigenvalue and eigenvectors of the Hamiltonian operator for the given system. This is a very difficult equation to solve as the eigenvectors (wavefunctions) and exact exchange-correlation functionals are unknown, and the overall equation requires a large number of operations to solve (at least $3\text{x}10^{23}$ for a single mole of an atom with only 3 degrees of freedom per atom). This is obviously impossible even with modern high-power computational facilities so, one may use the Kohn-Sham formalism of DFT to turn the many-body, many-interaction equation into a single-body, many-interaction equation.

First, since the nuclei of a solid tend to stay stationary about an equilibrium position they may be considered "clamped" in place. This implies that the nuclear and electronic terms in eq 2 may be separated where the nuclear portion is represented by a pseudopotential. The nuclei cannot be completely immobile due to the uncertainty principle, but this approximation holds as the motion of the electrons and nuclei happen on time scales many orders of magnitude apart and it is the electrons which contribute to

much of the physics of material science. The clamped nuclei approximation is more formally known as the Born-Oppenheimer approximation which effectively decouples the electronic and nuclear parts of the Schrödinger equation[33]. This simplifies eq 2 to the so-called electronic structure theory Schrödinger equation[21] given by,

$$\left[-\sum_i \frac{\nabla_i^2}{2} + \sum_i V_n(\boldsymbol{r_i}) + \frac{1}{2}\sum_{i\neq j} \frac{1}{|\boldsymbol{r_i}-\boldsymbol{r_j}|}\right]\Psi = E\Psi, \tag{3}$$

where atomic units are used such that $e = m_e = \hbar = 1$; the equation has simplified to sums over electronic coordinates.

In the initial solution to eq 2, the Coulomb term $\frac{1}{|\boldsymbol{r_i}-\boldsymbol{r_j}|}$ is neglected to treat the electrons independently. The probability of finding each electron at a point in space becomes a product of each individual (independent) probability such that $\sum_i^N \Psi(r_i, \dots, r_N) = \prod_i^N \phi_i(r_i)$. The independent electron approximation implies, similar to Hund's rule in chemistry, that the lowest energy configuration is the one where the lowest energy eigenstates (electrons) are filled first with a single electron before a second electron (of opposite spins) is added to an orbital.

To approximate an initial solution to eq 3, an ansatz must be guessed for the eigenfunctions (wavefunctions) of the Hamiltonian operator. To adhere to the Pauli exclusion principle where no two electrons may share the same set of quantum numbers, Slater determinants are used to construct the required anti-symmetric wavefunctions for fermionic species. The Pauli exclusion principle ensures that, when two electrons exchange their positions, their wavefunctions change sign, a natural property of determinants. The general slater determinant for N electrons is given by $\Psi(\boldsymbol{r_1}, \dots, \boldsymbol{r_N}) =$

$\frac{1}{\sqrt{N!}}\begin{vmatrix} \phi_1(\boldsymbol{r_1}) & \cdots & \phi_1(\boldsymbol{r_N}) \\ \vdots & \ddots & \vdots \\ \phi_N(\boldsymbol{r_1}) & \cdots & \phi_N(\boldsymbol{r_N}) \end{vmatrix}$. From this, the electron charge density may be constructed as a sum of the probabilities of electrons existing in the occupied states *i*, given by $n(\boldsymbol{r}) = \sum_i |\phi_i(\boldsymbol{r})|^2 = \sum_i \int \phi_i^*(\boldsymbol{r})\phi_i(\boldsymbol{r})d\boldsymbol{r}$. This density is at the heart of DFT calculations and only depends on the position of each electron.

The remainder of the formalism of DFT revolves around the Kohn-Sham equation, a modified and simplified, yet robust approximation to the many-body Schrödinger equation. The independent electron approximation is slightly relaxed, yet Slater determinants are still used to construct wavefunctions. Along with the Pauli exclusion principle, the Kohn-Sham equation includes the electron-nuclei interaction (Coulomb), the electron-electron interaction (Hartree-Fock) and the correlation potential which models the distance over which the strength of the electron's charge is felt by the neighboring electrons; the Pauli exclusion is modeled as the exchange potential. The full Kohn-Sham equation may be written as

$$\left[-\frac{\nabla^2}{2} + V_n(\boldsymbol{r}) + V_H(\boldsymbol{r}) + V_{xc}(\boldsymbol{r})\right]\phi_i(\boldsymbol{r}) = \varepsilon_i\phi_i(\boldsymbol{r}), \tag{4}$$

which does not seem like a simplification. However, this equation encapsulates everything required to accurately predict ground state properties using DFT and all terms are known except V_{xc}, the exchange-correlation potential. Numerous approximations have been developed that are either local, semi-local or non-local (range separated) where the further from local V_{xc} becomes, the more computationally taxing the calculations become.

The approximations for V_{xc} have improved over the last couple of decades from a mean-field approach using the local density approximation to modern meta-hybrid functionals which include an exact portion of exchange and an accurately approximated correlation potential. The most commonly used functional today within the computational code Vienna Ab-Initio Simulation Package (VASP) framework is the generalized gradient approximation (GGA) which improves upon the local density approximation by including the gradient of the charge density. To move beyond calculations of simple systems and study more complex material properties, hybrid functionals are employed to include the long-ranged interaction of electrons. A common hybrid functional is the Heyd-Scuseria-Ernzerhof (HSE06) screened Coulomb potential which includes short and long ranged electron interactions in the exchange potential[34]. The crux of all DFT calculations is finding the delicate balance between accuracy, level of theory and computational expense, where the latter is by far the largest bottleneck; however, computational power continues to improve, so it is only a matter of time before large-scale, exact modeling may be done.

2.3. Vienna Ab-Initio Simulation Package

Numerous software packages exist for DFT calculations, with VASP, although proprietary and somewhat expensive, leading the way in state-of-the-art periodic boundary condition DFT calculations. VASP uses the projector-augmented-wave (PAW) method which is an approach to setting up atomic wavefunctions which combines the pseudopotential and linear augmented-plane-wave methods; this method was developed to improve computational efficiency in DFT calculations. Due to the oscillatory nature of

valence-state wavefunctions near an ionic core, it is more suitable to transform the required orthogonal states into smooth functions e.g. polynomials; this can be done using a linear transformation that preserves addition and scalar multiplication. Thus, the PAW method uses pseudopotentials for the ionic cores within the frozen core approximation[35] and plane waves for the one-electron wavefunctions. The PAW method is used throughout this manuscript where VASP calculations are done.

VASP utilizes periodic boundary conditions to solve the Kohn-Sham equations to obtain the ground state eigenvalues and eigenfunctions of the system. Periodic boundary conditions are implemented using Blöch wavefunctions[36] which introduce the periodicity of the lattice through $\psi_k(\boldsymbol{r}) = e^{i\boldsymbol{k}\circ\boldsymbol{r}-\boldsymbol{\omega t}}\, u_k(\boldsymbol{r})$ where k is the crystal wave vector[37] in inverse angstroms, ω is the angular frequency in radians per second, t is time in seconds, and u($\mathbf{r}$) is the Blöch function with periodicity $u_k(\boldsymbol{r}) = u_k(\boldsymbol{r} + \boldsymbol{T})$; T is the translation lattice vector given in the basis of the unit cell. The exponential term above is an envelope function which encompasses the periodic function like the model in fig 4; this is the projection of the real part of the complex valued wavefunction at $\omega t = 0$.

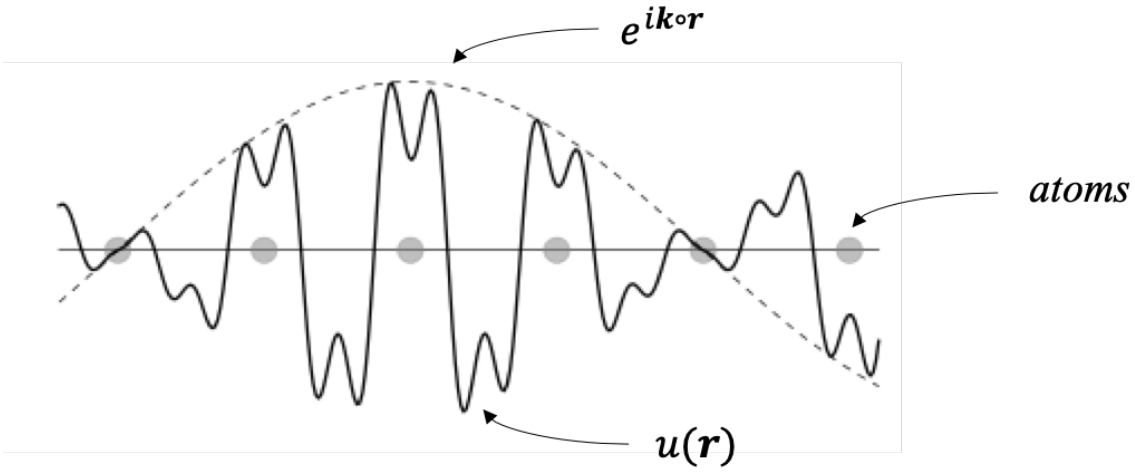

Figure 4. Toy model of a Blöch function. The exponential part is given as the dashed line and the periodic part is the solid line, which is periodic about the atoms of the lattice, given by the gray circles.

2.4. Density Functional Theory Applied

Most material studies start with optimization of the mathematical parameters required to solve the Kohn-Sham equations; these are done systematically, varying only one parameter at a time while holding others fixed at 'ideal' values. The size of the mesh in DFT calculations is determined by the number of k-points used which is based on the size of the system. The reciprocal space transformation is a clever formulation that results in the number of mesh points decreasing when the system size increases. Each k-point is defined as the projection of the real space vectors which define the material's geometry divided by the volume of the real space unit cell; here, a unit cell is defined as the smallest volume which, when replicated through space, creates the crystal structure of the material. For example, the k points in the x direction may be given as a multiple of $k_x = \frac{\vec{a}_y \circ \vec{a}_z}{\vec{a}_x \circ |\vec{a}_y \times \vec{a}_z|}$, where each $\vec{a}$ vector is a real space lattice vector in the given direction

(x, y, or z), and the subsequent k points in the y and z direction are obtained by cyclically permuting the indices of the numerator. Therefore, the first step in most DFT calculations is to optimize the number of k-points needed to give an accurate ground state energy while not being too computationally taxing. To do this, one picks a geometry for their crystal structure, which is the ideal geometry, and uses simple, default inputs to obtain the ground state energy of the ideal system. This is repeated for multiple k-point meshes until the lowest ground state energy is realized; it should be noted that increasing the size of the k-point mesh will decrease the ground state energy, but only up until a certain size where exponential behavior occurs. In other words, the right k-point mesh size is the one where the ground state energy converges to a value, and the change in ground state energy between increases in k-point mesh size is small (~0.01-0.10 eV). As with all parts of a DFT calculation, the crux of the problem is in finding the right level of theory to obtain accurate results within the given computational limits of the project.

The second part of a DFT calculation to be optimized after k-point mesh size is the basis set size given in eV and set using the ENCUT tag in VASP; the ENCUT value is the largest energy included in the basis. The basis set is a familiar feature of quantum chemistry and solid state physics calculations where either atomic orbitals or plane waves are used to represent the eigenvectors (wavefunctions) of the Schrödinger equation in reciprocal space, respectively; since this manuscript focuses on DFT (periodic boundary conditions) calculations, a plane wave basis set is used throughout. The largest default value of ENMAX given in the atomic pseudopotential files is sufficient for atomic or molecular studies but is often incorrect when crystal structure and volume optimization is required. Thus, for material studies where structural relaxations are done, the basis set

must be optimized. Once the correct k-point mesh is determined, this is used along with the ideal geometry to determine the basis set size. One may take 0.8 times the largest ENMAX value as a starting point and increase the basis set by 10-20 eV until an energy minimum is determined. Just like the k-point optimization, this is determined once the energy begins to converge and the difference between the ground state energy of two calculations is small. Often, the value of ENCUT is 1.2-1.3 times larger than the largest ENMAX value to account for Pulay stresses, a consequence of the incompleteness of the basis set; the basis set cannot be infinitely large and thus is never fully complete. Here, complete refers to the mathematical definition of completeness where any point in the vector space of the system being studied may be written as a linear combination of basis vectors.

DFT calculations may be split into two primary categories: (1) self-consistent field (SCF) and (2) non-self-consistent calculations. Self-consistency refers to the requirement that the final charge density be solved for iteratively from an initial guess with a convergence criterion in between each step of the iteration. In essence, a self-consistent calculation provides a robust way to check the ansatz (initial guess) for the trial wavefunctions and charge density. With the use of single Slater determinants, the operator matrix is diagonalized to obtain the eigenfunctions (wavefunctions) and eigenvalues (energies) of the initial ansatz. The charge density from this is then used to update the potential energy terms which are each a functional of the charge density. This iterative, self-consistent cycle is repeated until energy convergence is obtained and is shown pictorially in fig 5.

Non-self-consistent calculations, on the other hand, do not update the charge density after each calculation. Instead, the charge density from a self-consistent calculation is used and only the momentum (k-points) and positions are changed; often, a line-method with points of high symmetry is chosen in non-self-consistent calculations for band structures and density of states calculations. Thus, non-self-consistent calculations use the self-consistent, optimized charge density to recalculate electronic states at high-symmetry k-points while the ions remain fixed and the Hamiltonian is created from the initial charge density.

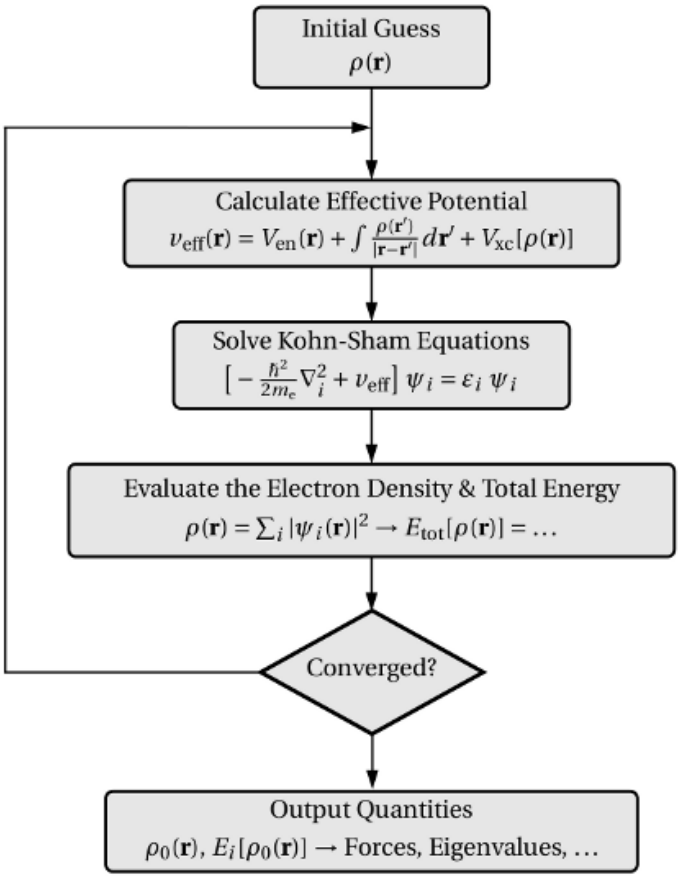

Figure 5. Schematic representation of the self-consistency cycle in Kohn-Sham density functional theory calculations. The arrow pointing back to the start of the cycle is a pictorial representation of the energy and force convergence criteria implemented in first principle calculations. The three dots in the fourth and sixth boxes indicate there are numerous terms that would not fit within the size of the box.

After optimizing the k-point mesh and basis set size, the next step is to optimize the lattice constant and volume of the crystal structure using self-consistent calculations. From these, one may obtain a volume-energy curve where the Birch-Murnaghan[38,39] equation of state may be fit to the data to obtain the equilibrium volume as well as the bulk modulus, a measure of the stress/strain that occurs when trying to deform a material, given by

$$E(V) = E_0 + \frac{9V_0B_0}{16}\left\{\left[\left(\frac{V_0}{V}\right)^{\frac{2}{3}} - 1\right]^3 B_0' + \left[\left(\frac{V_0}{V}\right)^{\frac{2}{3}} - 1\right]^2 \left[6 - 4\left(\frac{V_0}{V}\right)^{\frac{2}{3}}\right]\right\}, \quad (5)$$

where E_0 and B_0 are the energy and bulk modulus at the ground state volume V_0, respectively, and B_0' is the partial derivative of the bulk modulus with respect to pressure. The equilibrium volume may then be used as the starting point for the atomic relaxation calculations, where the volume and cell shape are fixed.

Ionic (atomic) relaxation is the next step in optimizing a crystal structure using DFT. Multiple algorithms have been developed to relax the ions of a periodic system into their instantaneous, equilibrium, ground state positions. However, the two most ionic minimization schemes used in VASP are the quasi-Newton algorithm called the residual minimization scheme with direct inversion in the iterative subspace or RMM-DIIS and the conjugate gradient algorithm. The RMM-DIIS algorithm is used when the initial geometry of the system is close to its equilibrium position. The conjugate gradient method, however, does not require the initial system to be close to equilibrium as this algorithm moves ions along the direction of steepest descent (the negative of the gradient). The initial result is then followed by as many line minimization steps that are required to ensure the forces of the final step are maximally orthogonal to the previous step, which is done through corrector steps within Brent's algorithm[40]. Figure 6 shows a toy model of the conjugate gradient method where each new search direction is conjugate to the previous direction. Each study detailed in the results and discussion section will indicate which method is used as different initial geometries lead to different convergence behavior for the energy and forces.

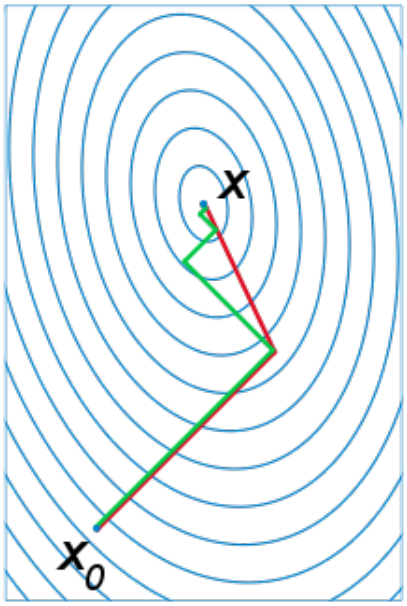

Figure 6. Conjugate gradient (red line) versus steepest descent (green line) method to minimize a function with initial guess x and minimum x_0. Blue lines are contours of a quadratic function.

The choice of exchange-correlation functional in these calculations is dependent on the balance between level of theory and computational resources available. Until recently, the hybrid functionals used for exchange-correlation potentials were computationally prohibitive for all but those with access to large, high-power computing facilities. Thus, other methodologies have been developed to "mimic" hybrid functionals by matching linearly the forces between the mimic method and the hybrid functionals as well as comparing parameters like the electronic band gap to experimental values. A useful method which has been proposed is the Hubbard correction which adds a penalty to the total energy to force the occupancy matrix towards idempotency; in other words, the correction forces occupancy to either be fully occupied or fully unoccupied with no partial occupancies. This ensures cancelation of the self-interaction error inherent to

semi-local approximations to the exchange-correlation potential by adding a term to the ground state energy, given by

$$E_{DFT+U} = E_{DFT} + \sum_{\alpha} \frac{U_{eff}}{2} Tr(\rho^{\alpha} - \rho^{\alpha}\rho^{\alpha}), \quad (6)$$

where E_{DFT} is the ground state energy from a calculation using semi-local functionals, U_{eff} is the Hubbard scaling factor, which is parameterized to the system being studied, ρ is the orbital occupation matrix elements and α is the site index. The full Hubbard model uses ladder and number density operators, but is parameterized by a hopping value (t) and the Coulomb parameter (U) where the limit of $t << U$ is used in the DFT+U study in this manuscript; this limit is applied to favor more localized states, something that is not achieved with semi-local functionals alone. This method is especially useful when modeling charged unit cells where an electron is either added or subtracted, where the charge carrier is either localized or delocalized based on its energy and the constituent atoms around the charge. Density (occupation) matrix values are given by (in Dirac notation) $\rho(\boldsymbol{r}, \boldsymbol{r}') = \langle \boldsymbol{r}|\hat{\rho}|\boldsymbol{r}' \rangle$, where $\boldsymbol{r}$ ($\boldsymbol{r}'$) is the row (column) element of the density matrix.

The Hubbard correction was first implemented to model so called "strongly-correlated" materials where traditional local or semi-local exchange-correlation functionals tended to over-delocalize valence electrons; this is a well-known failure of standard DFT[41]. Dudarev et al. first implemented the Hubbard +U correction to the local spin density approximation (LSDA) to improve the correlation potentials for d-orbital electrons. Energy loss spectra are studied by comparing the density of states of the LSDA and LSDA+U methods to experimental transmission electron microscopy data.

Also, lattice constant, band gap, cohesive energy, and stress tensor values computed with and without a +U correction are compared to experimental data[31]. More recently, P. Erhart extended the +U correction to GGA exchange-correlation functionals to model polarons in oxide perovskites[42]. This method is extended to hybrid halide perovskites and will be detailed in the results and discussion section.

2.5. Beyond DFT

When studying materials that contain large atoms, the outer valence electrons spin and orbital angular momentum couple due to a relativistic effect called spin-orbit coupling (SOC). SOC occurs when the interaction of the spin, orbital motion and electrostatic field due to the nucleus interact to shift the energy levels of electrons near the Fermi level where electronic occupation probability is exactly half. This shifting is due to the lifting of degeneracy of the energy levels at the band gap edges (valence band maximum and conduction band minimum) as spin and orbital angular momentum are no long viable quantum numbers. Instead, an effective spin-orbital term is defined resulting in a correction to the Hamiltonian given by

$$H_{soc} \propto \vec{\sigma} \circ \vec{L} = \vec{\sigma} \circ (\vec{r} \times \vec{p}), \tag{7}$$

where σ is the Pauli spin matrices and L is the angular momentum defined as the cross product of the position (r) and the momentum (p). For materials with inversion asymmetry, SOC results in the Rashba effect, a momentum dependent excitation seen in experiments as polarity dependent photocurrent. The Rashba effect due to SOC in hybrid halide perovskites will be detailed in the results and discussion section.

Once the crystal structure of a unit cell is optimized, material properties may be studied using various methods during and post-processing. To begin a VASP calculation, four text files are needed to define the crystal structure and atomic basis, calculation inputs, k-point mesh, and pseudopotential file for the ionic cores. The crystal structure is defined by the POSCAR or "position-card" file (VASP is a FORTRAN 90 program) which defines the three primitive lattice vectors and the position of each atom (atomic basis). The INCAR or "input-card" file defines the inputs which tell VASP what type of calculation and how the calculation is parallelized, to take advantage of modern high-power computing. The KPOINTS file defines the k-mesh and can either be given as a range of values, discrete values only from the irreducible Brillouin zone or as points of high-symmetry for band structure/density of state calculations. Finally, the POTCAR or "potential-card" file is the concatenation of the pseudopotential files (provided by VASP) for each atom given in the POSCAR file; it is important that the order of atoms in the POSCAR and POTCAR match. The type of exchange-correlation must also be taken into account as the LDA and GGA pseudopotentials are offered with VASP, where the LEXCHG tag is changed for each atom in the POTCAR file e.g. for PBEsol GGA exchange-correlation, LEXCHG = PS.

The primary output files from VASP give a full account of the inputs and calculated values throughout the run. The OUTCAR or "output-card" file prints all inputs and all results from the calculations based on the NWRITE tag in the INCAR; NWRITE = 2 is used throughout this manuscript which prints electronic energy and convergence information at each electronic step and all other information after each ionic step. The EIGENVAL file is a separate output of the parsed energy (eigenvalues) for

each band at each k-point from the OUTCAR file. The DOSCAR is similar to the EIGENVAL except that it is the parsed density of states at each energy (eigenvalue). The EIGENVAL and DOSCAR files may be imported and visualized using the Matlab library Vasplab[43]. The charge density and wavefunctions from the calculation are printed to the CHGCAR and WAVECAR files, respectively and may be used in subsequent runs to start from pre-converged values. The eigenvalues and density of states are also printed to a .xml file output (vasprun.xml) which may be visualized using the p4vasp package. VASP also prints a file of the optimized geometry after each ionic step during relaxation (rewriting at each step) called CONTCAR; this file may be renamed POSCAR and used to continue a geometry optimization calculation. It is also beneficial to create bash scripts to automate many of the steps that are repeated throughout a study; this is, however, simply a personal preference. Other output files will be created based on the type of calculation and the inputs provided in the INCAR file.

From the EIGENVAL and/or DOSCAR files, one may determine the electronic band gap (E_g) from the difference between the highest occupied and lowest unoccupied molecular orbital energy levels. In semiconductor physics, these orbitals are also known as the valence band maximum (VBM) and conduction band minimum (CBM), respectively. Figure 7 shows a toy model for an electron band structure with nearly parabolic bands to illustrate the band gap. The band gap in a material may either be direct, where an excitation equal to the band gap will promote an electron directly from the VBM to the CBM, or the band gap may be indirect, where a secondary process like a thermal vibration (phonon) in the lattice is required to move the promoted electron into the CBM from the virtual state in which it is initially excited; the red line in fig 7b

labeled dk is the momentum required to shift the electron into the CBM, and the dashed arrow is the indirect gap. The real dispersion relationship may be plotted after a non-self-consistent calculation using a pre-converged CHGCAR file with a KPOINT file modified to only include points of high symmetry.

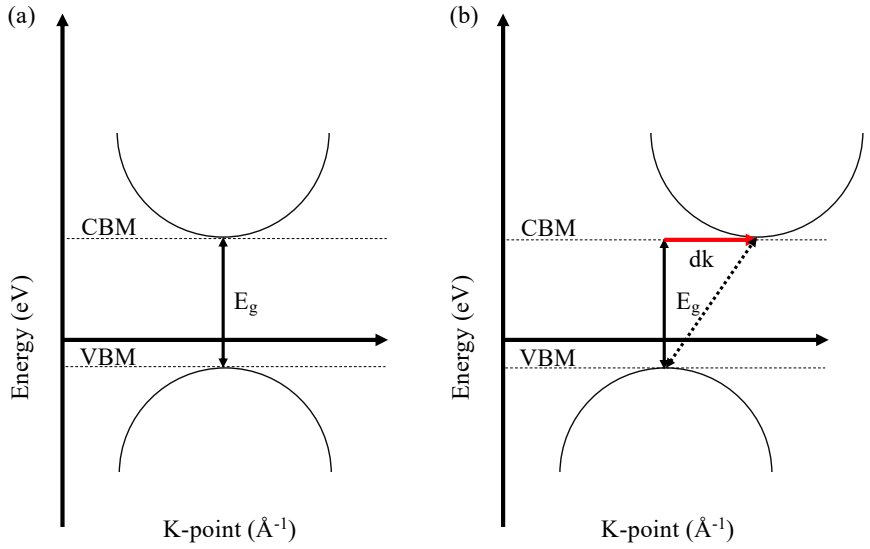

Figure 7. Toy model of electron band structure illustrating a (a) direct and (b) indirect band gap. The CBM and VBM occur at the same k-point (solid double arrow) in (a) while a process with momentum dk (red line) is required to promote the electron from the virtual CBM state (solid double arrow) to the real CBM (dashed arrow) in (b).

The band gap may also be obtained from the total density of states (DOS) by determining the energy difference between states at the gap edges around the Fermi level. The DOS may be spin-polarized or non-spin polarized based on whether or not the calculation is collinear (spin-orbit coupling included). The band structure and density of states may also be used to look for localized states in the band gap when studying defects.

Within DFT, one may do optical calculations to obtain the dielectric response of the system both for static and frequency dependent parameters like absorption,

reflectance, or energy loss spectra. Perturbation theory within DFT is used to calculate linear optical properties following the work of Gajdos et al[44]. Stricter convergence criteria is required for electronic optimization when calculating the static dielectric properties within the independent-particle approximation and local field effects with respect to the Hartree potential may be included using the random-phase approximation; static properties may also be calculated using finite differences where VASP calculates the derivative of the cell-periodic part of the Blöch orbitals with respect to k as $\frac{\partial}{\partial k}|\tilde{u}_{n'\boldsymbol{k}_j}\rangle$. Frequency dependent dielectric properties may also be calculated within VASP but require a pre-converged WAVECAR file with similarly strict electronic convergence to the static dielectric calculations (EDIFF = 10^{-8} eV); VASP suggests not to do static and frequency dielectric calculations simultaneously and therefore, these calculations are done separately in this dissertation where optical calculations are reported. To obtain the frequency dependent dielectric functions, one must optimize the number of empty bands required to simulate conduction bands in the material. This is straightforward as one may compare the value of the dielectric function at $\omega = 0$ to the static dielectric constant from the static dielectric calculations, increasing the number of bands until these values are reasonably similar. With the appropriate number of empty bands, VASP may calculate the imaginary part of the dielectric matrix by summing over the empty states using

$$\epsilon^{(2)}_{\alpha\beta}(\omega) = \frac{4\pi^2 e^2}{\Omega}\lim_{q\to 0}\frac{1}{q^2}\sum_{c,v,\boldsymbol{k}} 2w_{\boldsymbol{k}}\delta(\epsilon_{c\boldsymbol{k}} - \epsilon_{v\boldsymbol{k}} - \omega) \times \langle u_{c\boldsymbol{k}+e_\alpha q}|u_{v\boldsymbol{k}}\rangle \left\langle u_{v\boldsymbol{k}}\middle|u_{c\boldsymbol{k}+e_\beta q}\right\rangle, \quad (8)$$

where e is the charge of the electron, q is the incident wave Blöch vector, c and v are conduction and valence band states, respectively, w_k is the weight of each k-point where

all w_k sum to unity, $\epsilon_{c(v)\boldsymbol{k}}$ is the conduction (valence) band energy, and each u is the cell-periodic Blöch orbital. Then, using the Kramers-Kronig transformation[45] the real part of the frequency dependent dielectric matrix may be computed from the imaginary part with a principal value Cauchy integral of the form

$$\epsilon_{\alpha\beta}^{(1)}(\omega) = 1 + \frac{2}{\pi} P \int_0^{\infty} \frac{\epsilon_{\alpha\beta}^{(2)}(\omega')\omega' d\omega'}{\omega'^2 - \omega^2 - i\eta}, \tag{9}$$

where P is the principal value of the integral, i is the imaginary number and η is a complex shift factor in the Kramers-Kronig transformation that smooths the real part of the dielectric function[44]. The real and imaginary parts can then be transformed into the refractive index and extinction coefficients (n and k) which are measured experimentally using spectroscopic ellipsometry. From $\epsilon_{\alpha\beta}^{(1)}$ and $\epsilon_{\alpha\beta}^{(2)}$ one may get n and k using the formulas

$$n = \sqrt{\frac{\epsilon_1 + \left(\epsilon_1^2 + \epsilon_2^2\right)^{\frac{1}{2}}}{2}}, \tag{10}$$

and,

$$k = \sqrt{\frac{-\epsilon_1 + \left(\epsilon_1^2 + \epsilon_2^2\right)^{\frac{1}{2}}}{2}}. \tag{11}$$

Physical properties like phonon frequency spectra, atomic bonding, and surface and interface profiles may also be studied using DFT. VASP can be used to calculate phonon frequencies or a postprocessing program created by A. Togo called phonopy may be used. VASP has two main methods for calculating phonon frequencies: (1) finite

differences, or (2) perturbation theory. For both methods, the Hessian matrix of second derivatives of the energy with respect to the change in atomic position is calculated from ionic displacements in each cartesian direction; symmetry can reduce the computational load significantly by reducing the number of displacements to inequivalent directions. The finite difference method computes the derivatives of the cell periodic part of the orbitals as sums over occupied band, while perturbation theory is a sum over occupied and virtual (unoccupied) states. Phonopy is used in pre- and post-processing to calculate phonon frequencies. In pre-processing, the phonopy interface takes a single POSCAR and creates a number of copies with small, random displacements to the atomic basis. One then does a single SCF calculation with no ionic relaxation (NSW = 0) for each POSCAR and uses phonopy post-processing to create a file containing information on the calculated forces from each individual SCF calculation. From this FORCES file, one obtains force constants between each POSCAR image, as well as the density of states of phonon frequencies which can be plotted within the phonopy interface. From the density of states one can determine the fundamental longitudinal optical phonon frequency ω_{LO} which is used, for instance, to calculate the Fröhlich coupling constant when studying polarons[46].

Extending the basics of DFT from electronic and ionic minimization and perturbative corrections, one may study things like surfaces and interfaces where atomic bonding and charge redistribution may be used to determine viable device architectures. Supercell structures may be used where only one cartesian direction is elongated and either vacuum or another supercell are placed on top of the supercell; one uses a vacuum to study surface properties, and two supercells stacked are used to study interface

properties as shown in fig 8a and 8b, respectively. Methodology for calculating important parameters are elaborated upon in each section where surface/interface calculations are done.

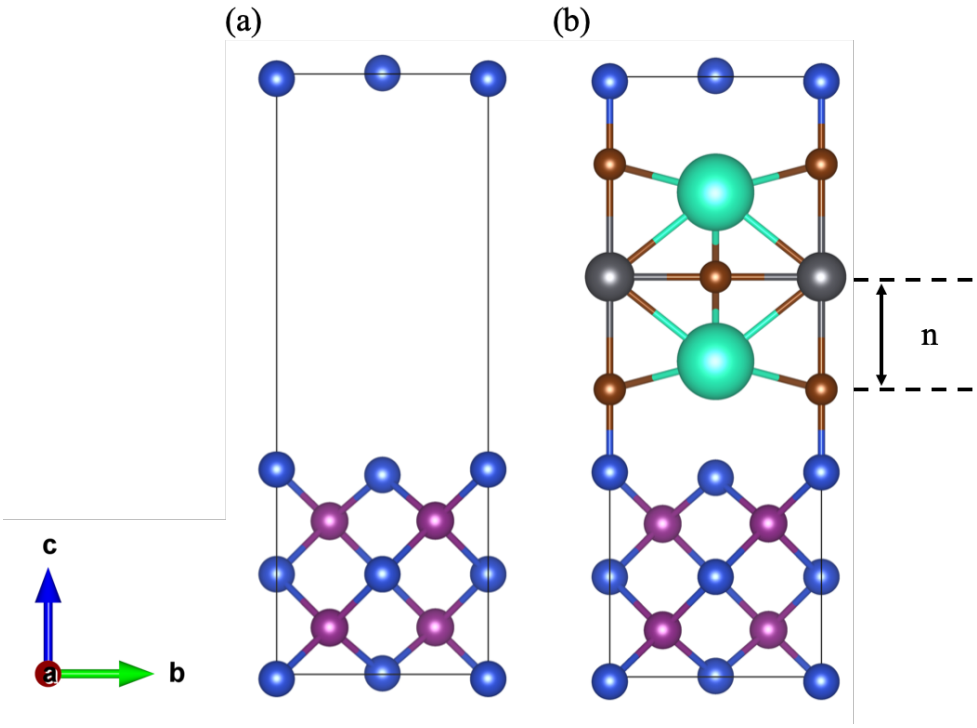

Figure 8. Surface model (a) with a vacuum above the surface, and interface model (b) between two separate materials. The value "*n*" represents an atomic layer which is increased to determine the effects of thickness on the local potential and charge density differences. Atoms are shown with different colors and size only as a model, not as any specific material (therefore colors are essentially irrelevant).

One thing to note about DFT is that it is a ground state property theory, meaning that excited state properties must be extrapolated from ground state calculations. There was once the misconception that DFT could *only* calculate ground state properties; however, DFT's true power lies in the fact that any property may be calculated given an appropriate functional which links the excited state to the ground state density[22]. Therefore, DFT may be used to calculate excited state properties like band structures,

density of states as well as the existence and potential localization of defects. Band structures computed using DFT show the discrete energy levels calculated at the specified level of theory coupled with an appropriate smearing method to approximate partial occupancies between the discrete energies. The "smeared" partial occupancy and discrete full occupancy energy levels are combined over a range of momenta (k-points) to form bands due to the large number of atoms in a crystal, which has been validated using experimental methods like angle resolved photoemission spectroscopy. These energies though are not the true Kohn-Sham quasiparticle eigenenergies, as approximation are made to the exchange-correlation potential which is notorious for miscalculating electronic band gaps. However, other approximation may be made to correct the total energy e.g. Hubbard correction, and will be discussed further in chapter 3. The reason the band structure is considered excited state in this context is due to the fact that the states in the conduction bands are virtual states. This means that DFT requires a ground state density determined from a self-consistent calculation which remains fixed during a non-self-consistent calculation to determine the energy values at (along) high symmetry k-points (lines) to extrapolate the conduction band energies. And, while there are an infinite number of energy bands, there are only a finite number of electrons to place in these energy bands based on the Pauli exclusion principle. Therefore, electrons must be promoted into the virtual states to determine the energy value at each k-point; this is unphysical in the sense that electron excitation occurs due to perturbative processes which require higher levels of theory like Green's function (GW) or $k \circ p$ perturbation theory[44]. It must be noted that band structures are calculated for the unit cell of a material; meaning, if a supercell is used, unphysical bands will exist due to band folding

from periodic boundary conditions and thus require band unfolding methods to return the band structure to the unit cell representation[36].

Lastly, charged systems may also be modeled in DFT using appropriate methods that take into account the interaction between a charge carrier and the ionic lattice. This is done using the Hubbard method known in literature as either the DFT+U or GGA+U method. In VASP, one may remove or add electrons, where removal effectively adds holes to the system. One may then compare a system with full valence, one with a charge added or removed from the ground state geometry, and one relaxed with a charge added or removed. VASP adds a background charge to account for the under/over-filled valence states. Polarons and the GGA+U method will be detailed more in the chapter 3.

3. RESULTS AND DISCUSSION

During the time the research was done in this manuscript, the Material Project[19] improved and increased the size of its database by orders of magnitude with accurate crystal structures for hundreds of thousands of materials. The unit cell lattice vectors and atomic basis for all structure (in .cif format) are taken from the Material Project database and then are visualized and converted into the VASP structure file POSCAR using the Visualization for Electronic and Structural Analysis (VESTA) package[47]; VESTA is also beneficial for converting a unit cell into a supercell and visualizing charge density and relaxation positions of atoms after a calculation. From that end, this chapter is broken down as follows: The first section of this chapter extends a method detailed in oxide perovskites to HPs to show the efficacy of the method to model polarons in HPs. The results of this modeling along with spin-orbit coupling effects led to the hypothesis of momentum dependent photoexcitation in devices which was tested in lab on HP devices using THz emission spectroscopy and is outlined in the second section of this chapter. The results of the measurements corroborated the calculations which were then followed by a study of the strength of the momentum dependent photoexcitation based on the stoichiometric ratio of the HP; this is detailed in section three of this chapter. The interface between an HP and an inorganic semiconductor is then studied to predict the viability of these two materials as an emissive and transport layer material in OE devices, respectively. Finally, a small review over the current state of polarons in HPs is given.

3.1. DFT+U Modeling of Hole Polarons in Halide Perovskites

Once perovskites were discovered to behave as efficient active layer materials in optoelectronic devices, research into fundamental photophysical processes were undertaken to explain device parameters. As solar cells were the first market into which HPs truly emerged, the predominant focus of this manuscript will be on photovoltaic device processes; however, the interface section will discuss emissive devices.

HP solar cells have shown a rapid improvement in device efficiency from 3% to over 25% in only ten years of research, where optimized devices show long charge carrier diffusion lengths ($l > 10\ \mu m$)[48], high carrier mobility ($\mu \sim 200 \frac{cm^2}{Vs}$)[49], while being produced by inexpensive, room-temperature, solution-processed precursors. Also, due to shallow acceptor/donor states near the band edges, HPs show an impressive tolerance to defects[50]. However, not all was positive; device stability in ambient conditions were and still are elusive. Thus, first principle calculations have been used in collaboration with experimental measurements to better understand how to engineer more efficient OE devices.

Degradation of HPs at room temperature in normal humidity conditions continues to prevent scalability and full commercial implementation. Two mechanisms were first postulated by experimentalists to explain degradation: (1) ionic migration, and/or (2) small polaron formation. Multiple studies have been done on ion vacancies and migration pathways[51–60]; however, the first study in this manuscript focuses on the second mechanism[61].

Polarons were first defined by Landau in 1933 as a charge moving through a lattice and the associated distortion due to the charge carrier i.e. phonon cloud[62]; the term

polaron was actually coined by Pekar over a decade after Landau's first paper. J. Devreese published a concise history of polaron theory in 2015 which references the seminal works on the theory of polaron formation[63]; translations of the original works may be found for some of these papers. Polarons in HPs will be summarized in the last section of this chapter.

Oxide perovskites were the first to be studied in the field, as $CaTiO_3$ was the first mineral discovered to possess the perovskite structure. Polarons were studied from first principles in the prototypical oxide perovskites $SrTiO_3$, $BaTiO_3$, and $PbTiO_3$, where the Hubbard model correction to the GGA (PBE) exchange-correlation functionals were shown to give results which are comparable to more accurate but significantly more computationally expensive hybrid functionals[20]. This method is extended to the halide class of HPs in the first study in the manuscript; due to the partial ionic nature of HPs, polarons are expected to exist in devices. Published in AIP Advances in 2016, it was shown that the GGA+U method can successfully model polarons in HPs[61].

First, a 6x6x6 gamma centered k-point mesh along with a kinetic energy cutoff of 500 eV was determined to be sufficient for unit cell calculations of ground state properties. The equilibrium, cubic lattice constant is found to be 6.3 Å (experimental value of 6.21 Å[64]), while the bulk modulus, determined from the 3rd order Birch-Murnaghan equation of state is 16.6 GPa (experimental value of 16 GPa[65]); PBE exchange correlation results in reasonably good approximations to the lattice constant and bulk modulus (< 1% error). Figure 9 shows the cubic structure of $MAPX_3$ with the MA dipole oriented along the c-axis.

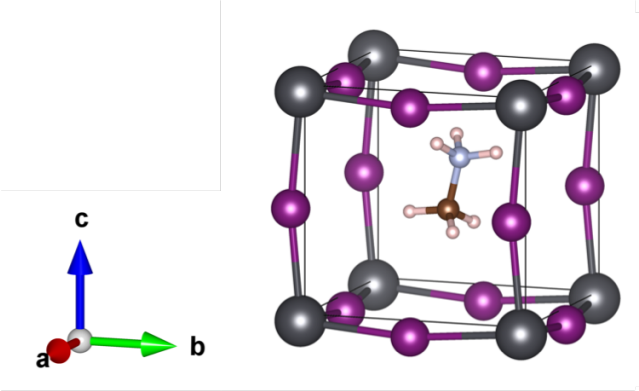

Figure 9. Optimized unit cell of $MAPX_3$ in the cubic structure. Small brown atoms are C, light-blue atoms are N, small pink atoms are H, large silver atoms are Pb, and purple atoms are the halide. Distortions in the Pb-halide cage are represented by purple-gray bonds between the Pb and halide atoms.

The band gap for cubic MAPI from PBE calculations is 1.2 eV. While this value is reasonably close to the experimental value of 1.51 eV[66], relativistic effects due to large atoms like Pb and I must also be included through the use of spin-orbit coupling (SOC) corrections, which will decrease the electronic band gap; SOC corrections result in degeneracy breaking as well as shifting of the band edge energies. Consequently, non-collinear calculations resulted in a band gap of 0.48 eV, nearly 1 eV smaller than without SOC. Also, the calculated Rashba parameter at the PBEsol+SOC level of theory is 0.13 and 0.2 for the conduction and valence bands, respectively, indicating that SOC results in momentum dependent photoexcitation due to inversion symmetry breaking in MAPI. The band gap has been improved using GW or hybrid functional calculations[67]. Figure 10a shows the band edges of MAPI without and with SOC corrections revealing the shift in the band edge energies as well as the degeneracy breaking leading to Rashba splitting; for reference, fig 10b shows $CsPbBr_3$ which has a strong band edge shift due to SOC in Pb (the dominant species contributing to the conduction band edge), but no Rashba splitting as there is no inversion symmetry breaking when the A site is an atom instead of

a molecular dipole. The effect of SOC in mixed metal and mixed halide HPs is shown in the next section.

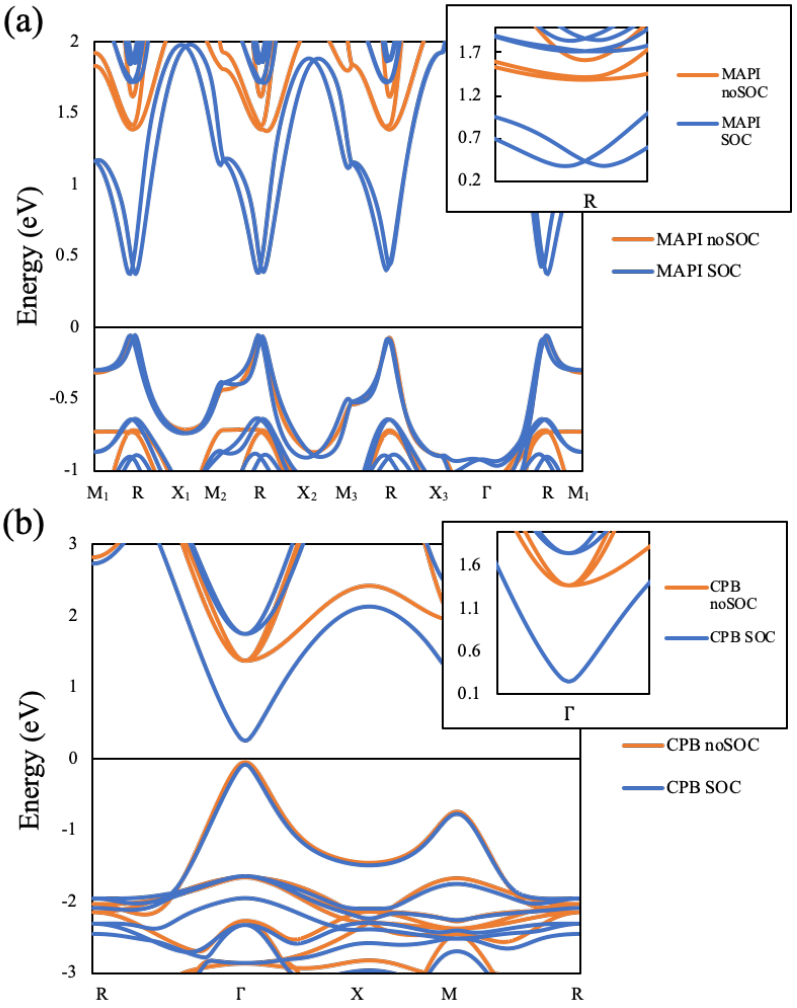

Figure 10. Electronic band structures without and with SOC corrections added for (a) $MAPbI_3$ and (b) $CsPbBr_3$. Inserts show the bands at the band gap near the conduction band edge to elucidate Rashba-type splitting.

The orbital contribution to the band edges in MAPI is shown in figure 11 to be hybridized bonding between I-p, Pb-p and Pb-s states at the valence band edge (at E = 0 eV) and Pb-p, I-p and I-s states at the conduction band edge (at E = 1.2 eV); this implies

that electronic and optical excitations occur almost entirely within the inorganic framework (PbI_6^{-4} sublattice).

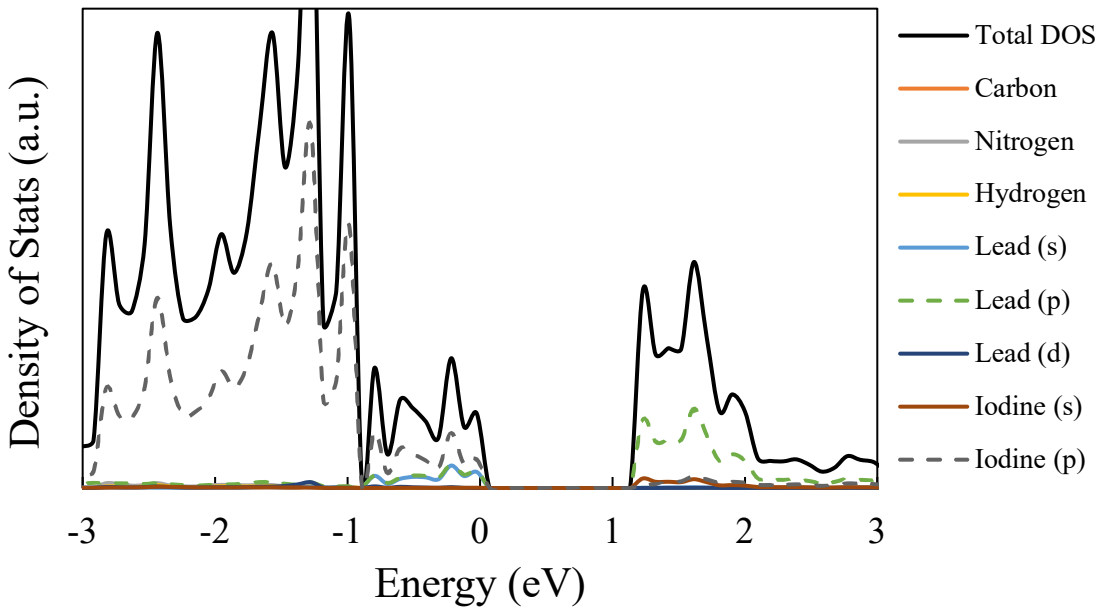

Figure 11. Partial density of states for MAPI showing orbital contribution to the band edges. The dominant orbital contribution to the valence and conduction band edges are shown as dashed lines.

Next, with the optimized cubic structure, hole polarons were studied by removing an electron and allowing the system to relax with the aim to search configuration space for any self-trapped holes. As is shown in fig 12 (blue line), PBE exchange correlation alone does not result in a polaronic state. Thus, the ground state, optimized geometry from PBE calculations was used to then find a Hubbard correction (U) value which could effectively cancel the self-interaction error from PBE alone. Single SCF calculations were done where the ions were held in place and the electronic ground state was reoptimized with a U correction added to the p-orbital of the halide; the p-orbital of the oxide in oxide perovskites was also used for this correction in previous work[20], and is the

most likely location for a hole polaron to localize. First parameterizing against the electronic band gap, a U value of 8 eV was found to result in the closest band gap value (E_g = 1.6 eV). This value was then used to relax the ground state neutral geometry with one electron removed to show that this U value resulted in localizing a polaron, manifesting as an electronic density within the band gap (red line in fig 12 below). It has been stated in the literature that if the U value is only used to improve the electronic band gap, then a scissor operator would be more suitable to shift the system eigenvalues to the correct values to match the experimental band gap; however, when looking to processes like catalysis or charge localization, the U parameter is tuned to the specific phenomenon which is being studied i.e. oxidation-reduction energy or localized density in the bandgap, respectively[68]. As this study was looking at more than just a correct band gap, the use of a Hubbard parameter is appropriate as the scissor operator only shifts the conduction band eigenvalues with respect to the valence band but does not remove double-counting/self-interaction from the semi-local exchange-correlation. Also, the U parameter effectively removes the double-counting error inherent in the self-interaction error of local/semi-local exchange correlation, which affects the shape of the band to which the U correction is added; in other words, the U parameter modifies the shape of frontier orbitals (band edges) in HPs. The forces calculated during electronic and ionic relaxation SCF calculations were then compared between GGA+U and HSE06 calculations for a single unit cell of MAPI to show a one-to-one relationship between the levels of theory. Adding hybrid functionals to the GGA+U calculation resulted in minimal improvements to the ground state energy (< 0.01 eV) of the fully relaxed MAPI

unit cell, indicating that the Hubbard parameter correction gives a reasonable approximation to the ground state geometry.

Electronic and dielectric values were calculated to study the Fröhlich model parameters to quantitatively predict the existence of polarons in HPs, except for the longitudinal optical phonon frequency which is computationally taxing; there have been some groups to report on these frequencies, but they are more likely to be explored using experimental spectroscopic methods. Thus, the phonon frequency used in the Fröhlich model is taken from experiment. As is shown in fig 12, no deep band gap state exists when an electron is removed from the system (creating a hole polaron) and PBE exchange-correlation alone is used to relax the system; in other words, PBE exchange-correlation delocalized free charge carriers due to self-interaction errors. The Hubbard correction accounts for the interaction between the ionic lattice and the mobile charge carrier as well as canceling the self-interaction error, which is not canceled in PBE exchange correlation, resulting in a localized state in the band gap.

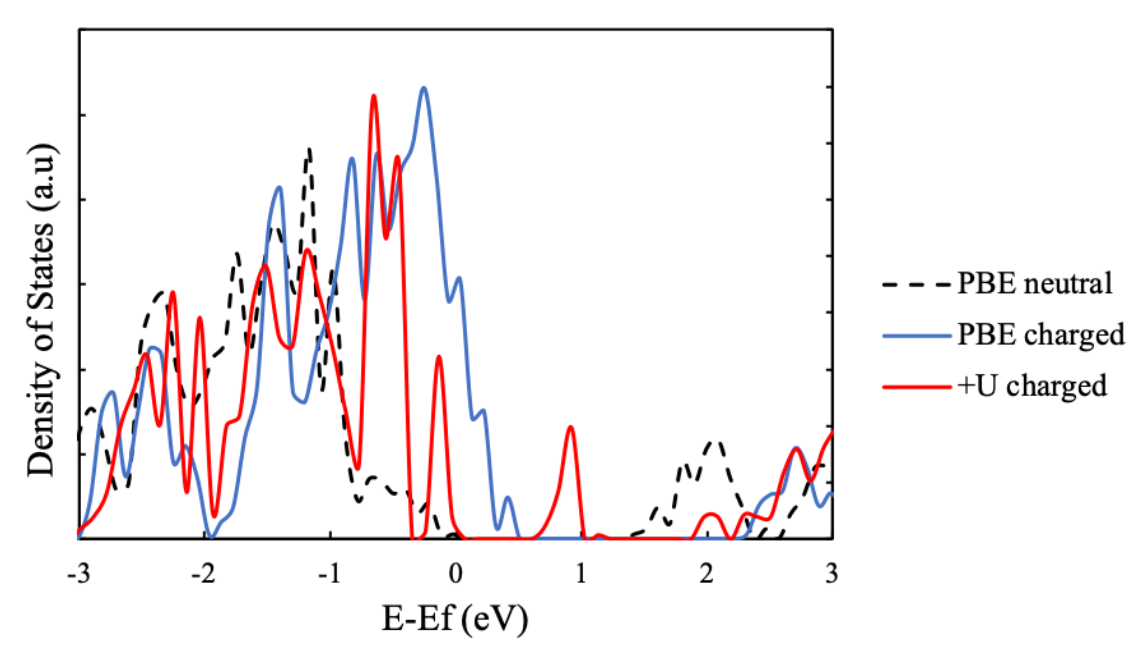

Figure 12. Total density of states for neutral and charged $MAPbI_3$ using PBE exchange correlation and charged $MAPbI_3$ using U = 8 eV on the p-orbital of iodine. Removal of an electron only shifts the band edges but does not localize the charge carrier in PBE, where the Hubbard correction realizes the localized deep band gap state and shifts the band edges closer to the neutral, U = 0 eV system.

The Fröhlich model was extended by R. Feynman[46] using a variational principle to determine the coupling constant of a slow-moving electron through a polar medium given by

$$\alpha = \frac{e^2}{\hbar c}\sqrt{\frac{m_b c^2}{2\hbar\omega_{LO}}}\left(\frac{1}{\epsilon_\infty}-\frac{1}{\epsilon_0}\right), \tag{12}$$

ϵ_∞ and ϵ_0 are the frequency and static dielectric constants from optical calculations, e is the charge of an electron, $\hbar$ is Planck's reduced constant, c is the speed of light in vacuum, m_b is the electron or hole effective mass, and ω_{LO} is the longitudinal optical phonon frequency. The term in front of the square root is the well-known fine structure constant which may be approximated as 1/137.

The Fröhlich coupling constant is large in ionic salts and small in inorganic semiconductors like GaAs and GaP[69]. M. Nagai et al. recently determined phonon frequencies for each halide HP using THz time-domain spectroscopy[70]. Table 1 summarizes the calculated values with SOC corrections (taken from the supplementary information of E. Welch et al.) as well as the experimental values from M. Nagai's work along with the calculated coupling constants for each pure halide system; the mixed halide values are not included as a phonon frequency for that material has not yet been measured.

Table 1. Fröhlich coupling constant parameters from DFT GGA+SOC+U calculations, experimental phonon frequency measurements, and calculated Fröhlich coupling constants for electron (α_e) and hole (α_h) polarons. The dielectric constants are in Farads per meter, effective masses are given as a ratio of the percent of the rest mass of an electron (and is therefore unitless), the longitudinal optical phonon frequency is in units of THz, and thus, the Fröhlich coupling constant is unitless.

Molecule	ϵ_0	ϵ_∞	m_e^*	m_h^*	ω_{LO}[70]	α_e	α_h
$MAPbI_3$	14.9	5.31	0.19	0.36	3.98	1.52	2.09
$MAPbBr_3$	8.0	3.84	0.22	0.11	4.86	1.65	1.17
$MAPbCl_3$	5.9	3.09	0.30	0.21	6.9	1.84	1.54

The static and frequency dependent dielectric constants are taken from density functional perturbation theory calculations[61], where the static dielectric constant is the trace of the three-dimensional dielectric tensor; the frequency dependent dielectric function is calculated and parsed into the real and imaginary parts as well as any off-diagonal terms in the OUTCAR file. The effective mass is found using the parabolic band fitting method which effectively fits a parabola to the band edge bands using

$$\frac{1}{m^*} = \frac{1}{\hbar^2}\frac{\partial^2 E}{\partial k^2}, \tag{13}$$

where the second derivative of energy with respect to momentum on a band diagram is mathematically termed the concavity of the graph which is positive for electrons and negative for holes; the absolute value for the effective masses is reported in Table 1.

The calculated values for the three pristine halide perovskites are similar to reported values[71] and lie just below the strong coupling regime $\alpha \geq 5$. This indicates that polarons are expected to exist in devices and require the balance of small polaron mitigation and large polaron engineering. Hole polarons are in fact seen in each of the HPs studied as a band gap state in the electronic dispersion relation (band structure) near the highest occupied molecular orbital (valence band maximum).

It was suggested by one reviewer of this work pre-publication that spin-orbit coupling was important and should be included. This was the first time the author learned of SOC and thus, after understanding the heuristic side of the model, SOC corrections were implemented and all calculations were redone using the relativistic corrections to account for the presence of heavy Pb and halides. Interestingly, polaronic behavior was still seen in each of the systems using SOC corrections. This was argued to occur due to the fact that SOC is much stronger in the conduction band comprised of Pb, than in the valence band comprised of a halide, and this study focused on hole polarons which are semi-localized in the p-orbitals of the halide. Since the valence band was not significantly affected by SOC corrections, the hole polaron wavefunction still found a low energy surface onto which to partially localize in the band gap near the VBM.

The DFT(GGA)+U method was used to successfully realize hole polarons in halide perovskites while minimizing the computational cost required by hybrid

functionals. The Hubbard (+U) correction is parameterized to approximate electronic and dielectric properties to quantize hole polaron behavior. The Fröhlich model for polarons shows that both pristine (halide-only) and mixed-halide HPs expect moderate electron-phonon coupling with semi-localized band gap states existing in the total density of states both with and without SOC corrections. Plotting the partial density of states as a function of energy reveals that the band edges are comprised of Pb (CBM) and halide (VBM) p-orbitals, where the SOC corrections are expected to be most prominent; the halide p-orbital is also where the Hubbard correction is added as the halide is the most likely trapping sight for small hole polarons. For the pristine halide HPs, the (hole) acceptor level moves further from the VBM as the halide decreases in size while the band gap increases with decreasing halide size. Dielectric constants follow the trend of the polaron level, decreasing as the halide size decreases. This work coupled with those in the field at that time show that the true power of HPs in OE devices is in the tunability of OE properties through atomic mixing. This will be further emphasized in section 3.3 when the strength of SOC is measured for mixed metal and mixed halide HPs to predict optoelectronic/opto-spintronic applications.

3.2. Spin-Orbit Coupling, Rashba Splitting and the Circular Photogalvanic Effect in Devices

Looking at the effect of SOC on HPs, the split seen at the band gap k-point is studied using the Rashba model[72] to determine how much the direct band gap without SOC changes into an indirect band gap with SOC. Figure 13 shows a toy model of what occurs as the degeneracy of a band is lifted due to SOC, where the single parabola at the

VBM/CBM becomes two parabolas shifted in momentum by Δk. The effect of this splitting can be quantified by the Rashba parameter given by

$$\alpha_R = \frac{2\Delta E}{\Delta k}. \tag{14}$$

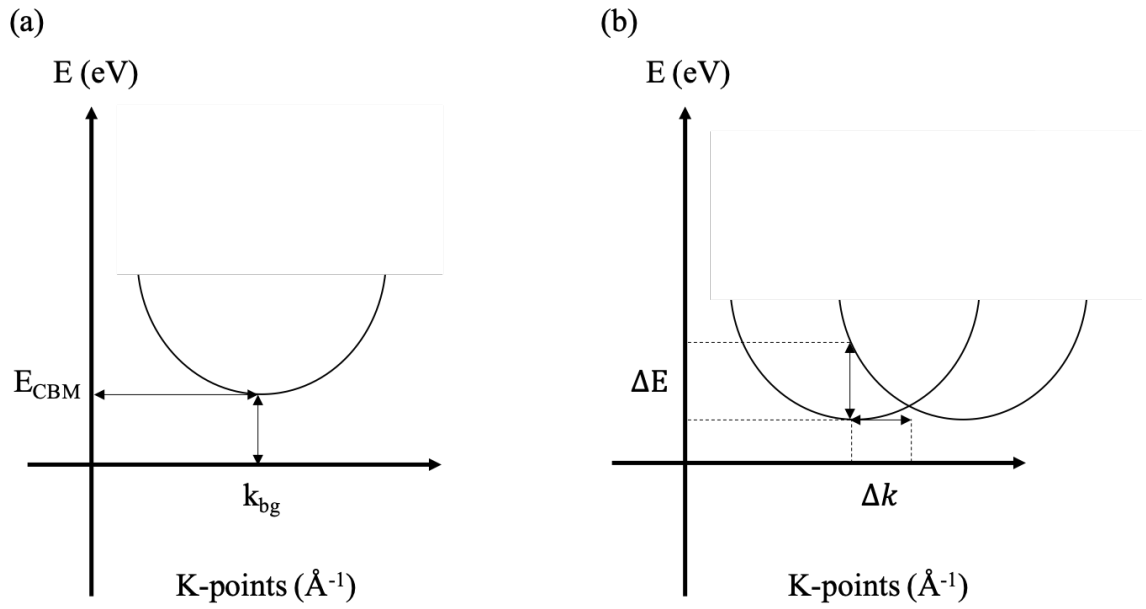

Figure 13. Toy model for conduction band minimum at the band gap for a system without (a) and with (b) spin-orbit coupling. For a material with a direct band gap, the conduction band minimum energy (E_{CBM}) occurs at the band gap momentum (k_{bg}) where the valence band maximum energy also occurs. ΔE in (b) is the difference in energy between the conduction band minimum of one split-off band and the energy at the same k-point of the adjacent split-off band. Δk is the difference in momentum between the direct band gap and the split-off band minimum.

A larger Rashba splitting parameter (α_R) indicates a smaller difference in momentum between the minimum of the split-off band from SOC corrections and the CBM/VBM of the system without SOC corrections; this indicates the shift to momentum dependent excitation due to SOC is less pronounced when α_R is large. Conversely, when α_R is small, photoexcitation is strongly dependent upon the momentum of a

photoelectron, which implies the existence of the circular photogalvanic effect (CPGE) in experiment. This effect occurs when incident photons of different polarization (left or right-handed) result in a photocurrent which propagates in a different, polarization dependent direction. Since HPs show an anharmonic electron dispersion relation, the Rashba splitting parameter is averaged over the k-points which relate, in real space, to the high-symmetry (100), (010), (001), (110), (011), (101), and (111) directions; this is done for both the CBM and VBM. Focusing on two of the pristine halide HPs ($MAPbX_3$ where X = I, or Br), SOC is predicted to have the greatest effect in I based HPs and will decrease for Br as the halide gets smaller; other, non-pristine (mixed) HPs are discussed in the next section. And, in fact, $MAPbI_3$ has calculated Rashba splitting parameters of (VBM) $\alpha_{R_v} = 0.00\ \frac{eV}{\text{Å}}$ and (CBM) $\alpha_{R_c} = 0.131\ \frac{eV}{\text{Å}}$, whereas $MAPbBr_3$ has $\alpha_{R_c} = 13.898\ \frac{eV}{\text{Å}}$ and $\alpha_{R_v} = 11.265\ \frac{eV}{\text{Å}}$, both calculated at the GGA+SOC+U level of theory with U = 8 eV added to the p-orbital of the halide atom. This result led to our experimental group creating high-quality devices to send to collaborators in Japan and Russia to do THz emission spectroscopy experiments to test the hypothesis of SOC effects leading to the CPGE.

The experiments used to probe picosecond, transient behavior (time scale where electron-phonon coupling and SOC are probed) were photocurrent response and THz emission measurements. A summary of these experiments done by colleagues in Japan and Russia follows[73]:

The transient photocurrent, a measure of the extraction of excited charge carriers due to incident light, was measured using a Coherent Elite Pro Ti:Sapphire amplified system. Both pulsed and continuous wave lasers were used to measure the dependence of

photocurrent on the wavelength of incident radiation; the sample was unbiased and measured at room temperature. A four-component oscillator model is used to fit the photocurrent data where the terms help to differentiate between circular and linear polarization dependent photocurrents, given by

$$J(\alpha) = D + Csin(2\alpha) + L_1 \cos(4\alpha) + L_2 \sin(4\alpha). \quad (15)$$

In this equation, α is the angle of the quarter-wave plate used to vary the polarization of the incident laser, D is an offset attributed to heat in the sample, C is the strength of the circular polarization component in the photocurrent, and L_1 and L_2 parameterize the linear polarization components of the photocurrent. A strong circular polarization dependence is seen in the photocurrent for the unbiased thin film MAPI samples with a contribution of almost 70% to the total photocurrent detected on a 600 MHz digital oscilloscope.

Time-resolved THz emission spectroscopy was also used to measure the polarization dependent photocurrent after excitation from femtosecond laser pulses. A standard electro-optical sampling method was used where a Yb:KGW diode-pumped laser was incident upon the sample with femtosecond pulses and gold, parabolic mirrors were used to measure emission. Upon excitation, ultrafast photocurrents are generated in the material which are polarization dependent, one sign of the CPGE. THz emission from the films after excitation also indicates a break of inversion symmetry in MAPI, another sign of the existence of the CPGE. Since electron-phonon coupling results in a partially localized, band gap state even when SOC corrections are included in calculations, the emission of THz emission in experiment points towards photoinduced

polarons resulting in expansive lattice distortions. These experimental results coupled with the DFT calculations indicate the presence of small polarons in HPs.

The results from the DFT calculations in section 3.1 led the experimental team of Dr. Alex Zakhidov at Texas State University to make devices which were tested in Japan and Russia using THz spectroscopy experiments. These experiments were used to probe picosecond, transient behavior in an attempt to determine the nature of inversion symmetry breaking in HPs due to rotational dynamics and trapped states (polarons) as well as the existence of the CPGE due to momentum dependent excitations from SOC. Momentum dependent, ultrafast photocurrent generation confirms both inversion symmetry breaking and the CPGE in thin film HP solar cells, revealing the promising potential of HP implementation in spin-controlled OE devices. The experimental results are elaborated upon in appendix A.

3.3. Effects of SOC on Mixed Perovskites and Possible Optoelectronic/Spin-Optoelectronic Applications

To build upon the work with pristine halide HPs, the perovskites $MAPb_{1-x}Sn_xBr_{3-y}I_y$ with $x = 0$, 0.375, and 0.625 (the decimals are 3/8 and 5/8, the ratio of each metal to the total metal atoms; in other words, Pb_5Sn_3 or Pb_3Sn_5) and $y = 0,1,2$, and 3 are studied. These ratios are used due to the size of and number of atoms in the supercell. The choice of which atom was chosen to be Pb/Sn or I/Br in the mixed systems was randomized using atmospheric random number generation (sequence generator at random.org) to ensure the most random dispersion of atoms in the mixture; the total number of each atom was denoted a numerical value starting going from *1* to *n*, where the values *1* to *n*

were then randomized and assigned to the atomic basis value for each atom. While the system has less than 100 atoms and is thus highly unphysical, the system size used was sufficient to ensure randomization of the atoms used in the simulation box. Using 2x2x2 supercells, the ions of each system were relaxed into their instantaneous ground state using GGA exchange-correlation with and without SOC corrections to compare electronic band gaps and Rashba splitting parameters for systems with SOC corrections. The band gaps are calculated after convergence criteria of 10^{-6} eV and 10^{-5} $\frac{eV}{\text{Å}}$ for electronic and ionic relaxation is met, respectively; the band gaps for systems with and without SOC corrections and the Rashba parameters for systems with SOC corrections are summarized in Table 2. As in the pristine systems, the conjugate gradient method is used to find the ground state atomic geometry while a Hubbard correction is added to the p-orbitals of each halide. As is often the case, it is argued here that due to computational limitations, hybrid functionals for large, complex HPs is prohibitive. Thus, the Hubbard model is used and is, from section 3.1, considered adequate for comparison of the trends in electronic and optical behaviors.

Table 2. DFT calculated band gaps with and without SOC corrections and average Rashba splitting parameters for the valence and conduction band edges.

System	E_g no SOC (eV)	E_g with SOC (eV)	dE_g (eV)	α_{R_v}	α_{R_c}

$MAPbI_3$	1.650	0.750	0.910	0.00	0.13
$MAPbI_2Br$	2.003	0.814	1.189	15.07	31.39
$MAPbIBr_2$	2.114	1.022	1.092	6.85	18.80
$MAPbBr_3$	2.509	1.536	0.973	13.90	11.26
$MAPb_5Sn_3I_3$	1.187	0.535	0.652	14.14	23.29
$MAPb_5Sn_3I_2Br$	1.478	0.739	0.379	15.12	27.64
$MAPb_5Sn_3IBr_2$	1.805	0.981	0.824	13.65	14.08
$MAPb_5Sn_3Br_3$	2.328	1.530	0.798	16.50	10.98
$MAPb_3Sn_5I_3$	1.088	0.642	0.446	50.19	20.84
$MAPb_3Sn_5I_2Br$	1.642	0.739	0.903	10.30	16.13
$MAPb_3Sn_5IBr_2$	1.605	0.977	0.628	11.06	11.70
$MAPb_3Sn_5Br_3$	2.122	1.529	0.593	0.96	0.49
$MASnI_3$	0.990	0.749	0.241	55.88	81.85
$MASnI_2Br$	1.195	0.971	0.224	21.76	29.18
$MASnIBr_2$	1.502	1.313	0.189	10.50	14.83
$MASnBr_3$	1.960	1.864	0.096	15.91	7.28

The smaller Rashba parameter for MAPI and $MAPb_3Sn_5Br_3$ indicates that these two materials will likely exhibit a strong CPGE when used in an OE device and will see the largest amount of inversion symmetry breaking; spintronic devices like ultrafast photodetectors[73] may be realized from HPs that show the largest amount of Rashba splitting. Almost all other systems have moderate Rashba parameters, except two systems, which have the largest two Rashba parameters: the Sn-dominant, I_3 systems. As Sn is smaller than Pb, SOC is less pronounced and thus, Rashba splitting is also less

pronounced. The systems with moderate Rashba splitting ($5 \leq \alpha \leq 25$) have the potential to be used in applications like spin-LEDs and spin-valves which can be used to probe the fine structures of excited states by exploiting the Hanle effect which demonstrates spin injection and transport through an HP layer. HPs may be used in devices with ferromagnetic anodes and metal cathodes, where holes and electrons are injected into the HP layer to form excitons which bind and recombine based on optical selection rules[74].

In future studies, the effects of SOC on optical properties will be measured using conventional methods in VASP to determine the static and frequency dependent dielectric responses for each system. SOC corrections are required to lift the degeneracy in the bands at the conduction and valence band edges where optoelectronic transport occurs. Therefore, it is expected that SOC will enhance features in the absorption spectra for each material near the band gap, becoming more influential in systems where Rashba splitting is strongest such that photoexcitation becomes strongly momentum dependent. SOC noticeably decreases the electronic band gap upwards of more than 1 eV in these mixed halide HPs, which indicates the same may be true of the absorption band edge in the frequency dependent dielectric functions.

3.4. Interface Study Between HP and Inorganic Semiconductor

Turning from single system studies, the interface between $CsPbBr_3$ and CuI is studied for light emitting device applications using DFT methods; both $CsPbBr_3$ and CuI are inexpensive materials with promising HP OE device properties. The inorganic halide perovskite $CsPbBr_3$ has gained interest due to its attractive properties as an emissive layer

in LEDs. As noted before, perovskites require transport layers to create devices where materials are chosen to either extract or inject mobile charge carriers; in the case of an LED, the transport layers would inject mobile charge carriers into the emissive layer. The transport material of interest is the inorganic, wide-band gap semiconductor CuI, which has been used as a transport material for optically absorbing applications and is hypothesized as a cheaper alternative to current transport layer materials.

DFT calculations help to quantify the band offset type in an attempt to predict whether $CsPbBr_3$ and CuI may be used to create efficient LEDs, with CuI injecting holes into the $CsPbBr_3$. The interface between $CsPbBr_3$ and PbS was studied in a previous report for similar applications, and their method is adopted here[75].

The bond cleaving method to model semiconductor interfaces, summarized by J. Park[76] is used to calculate the energy required to add/remove a single layer of atoms. From this, one can study the charge density redistribution and low-energy atomic configuration of a surface, and then between interfaces. The charge density difference between the interface and the two separate materials as surfaces interfaced with vacuum shows the influence of the interface and predicts the stability of each atomic bonding arrangement.

First, the crystal structures are optimized for the 5 atom cubic $CsPbBr_3$ and 8 atom zinc-blende CuI unit cells using PBEsol exchange correlation. 6x6x6 and 10x10x10 gamma centered k-point meshes are used for $CsPbBr_3$ and CuI, respectively. A kinetic energy cutoff of 700 eV is used throughout the calculations. The optimized lattice constants, band gaps and bulk moduli are summarized in table 3. The third order Birch-Murnaghan equation of state is used to determine the bulk modulus of each

structure. As CuI has a larger bulk modulus, interfacial growth will be modulated by the CuI lattice parameters; thus, all interface areas for both materials are set to 35.28 $Å^2$ (5.94 squared), that of CuI. The band gaps of both materials are incorrectly predicted due to a lack of SOC corrections and hybrid exchange-correlation where inclusion of both resulted in a bandgap of 2.23 eV in $CsPbBr_3$; SOC and hybrid functionals are not included in the interface study however as the increase in system size causes computational cost to become prohibitive (HSE relaxation takes 300 times longer than PBEsol relaxation for a simple cubic system with 5 atoms). It has been shown in DFT studies of HP materials however, that the trends using only PBEsol exchange-correlation are still meaningful and predictive[77].

Table 3. PBEsol optimized physical constants for $CsPbBr_3$ and CuI unit cells. Values in parenthesis are experimental values.

System	Lattice constant (Å)	Band gap (eV)	Bulk modulus (GPa)
$CsPbBr_3$	5.88 (5.87)	1.41(1.73[78])	21.56 (15.5[79])
CuI	5.94 (6.02)	1.67 (3.1[80])	47.46 (36.6[81])

Next, the atomic arrangement is determined for the $CsPbBr_3$ and CuI low energy (100) surfaces. $CsPbBr_3$, in the cubic phase, has two unique atomic layers which both may form at the interface as either CsBr or $PbBr_2$. CuI, in the γ-cubic phase, also has two unique atomic layers, either all Cu or all I. Both $CsPbBr_3$ and CuI are charge neutral and thus both form type 1, non-polar surfaces. As each layer of $CsPbBr_3$ has two different atoms, there are a total of 8 interface bonding configurations which must be

studied as a surface interfaced with vacuum. The amount of vacuum is determined iteratively, where the appropriate ensures no interactions between adjacent unit cells in periodic boundary condition calculations.

The bond cleaving method uses the energy of the unrelaxed, ideal surface geometries for each termination and the energy of the relaxed bulk structure to calculate the cleaving energy given by

$$E_{cl} = \frac{1}{4A}[E_{slab}^{unrel}(t_1) + E_{slab}^{unrel}(t_2) - \frac{N_{slab}^{atom}(t_1)+N_{slab}^{atom}(t_2)}{N_{bulk}^{atoms}}E_{bulk}]. \quad (16)$$

Here, A is the area of the interface with a factor of ¼ due to two identical interfaces (four surfaces) in the slab model. The first two terms in the bracket are the energy of the unrelaxed (ideal) surface slab for each termination, N is the number of atoms for the two slab terminations and the bulk, and E_{bulk} is the ground state energy of the bulk unit cell. It should be noted that all absolute energy calculations are sensitive to the level of theory used during calculations, where ground state energies between semi-local and non-local exchange correlation functionals can be different by several eV.

Surface energy calculations reveal the lowest energy atomic layer by comparing the interface of each surface interfaced with a vacuum large enough to ensure that adjacent, periodic cells don't interact; a minimum of 15Å of vacuum (for a volume of at least 530 $Å^3$) is used throughout the surface calculations. Figure 14 shows the two unique surfaces of $CsPbBr_3$ (CsBr and $PbBr_2$ surfaces) and the two unique surfaces of CuI (Cu and I surfaces) as well as the bulk structures for each.

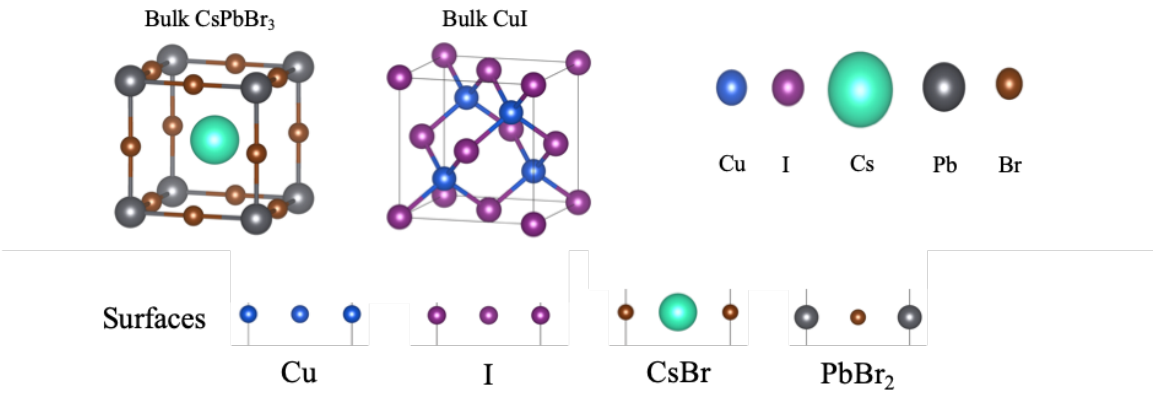

Figure 14. Bulk structures and unique surface terminations for $CsPbBr_3$ and CuI. Surfaces are viewed from the side, parallel to the (001) plane.

The surface energy for each termination is given by

$$E_{surf}(t) = E_{cl} + E_{rel} = E_{cl} + \frac{1}{2A}(E_{rel}(t) - E_{unrel}(t)), \quad (17)$$

where A is the surface area, the unrelaxed energy (E_{unrel}) is from a single point electronic SCF calculation, the relaxed energy (E_{rel}) is from the full ionic and electronic relaxation calculation, and t is the given surface termination; ½ is due to the two different surfaces. The thickness of each material is increased to distinguish any size effects and each calculation is repeated for 5, 7, and 9 atomic layers of $CsPbBr_3$ and 9, 13, and 17 atomic layers of CuI, which equates to 2, 3, and 4 unit cells of each material; this is summarized in fig 15.

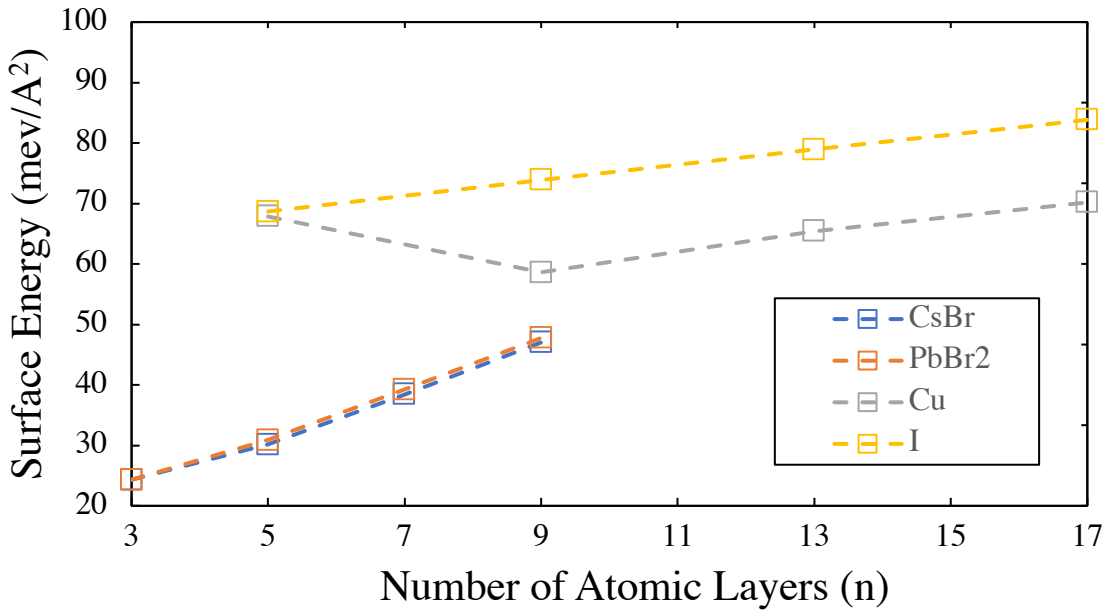

Figure 15. Surface energies for $CsPbBr_3$ and CuI as a function of increasing layer thickness.

CsBr and Cu surfaces are found to have lower surface energies for all thicknesses, distinguishing surface energy as a parameter that does not seem to depend on the thickness of the material (within some limit of course). The relaxed slab energies are also used in the interface calculations.

Eight unique interfaces exist between $CsPbBr_3$ and CuI. From intuition, a stable interface should at a minimum contain bonds between cations and anions, where a cation-cation or anion-anion bond is not favored due to electrostatic repulsion. Looking at the eight interfaces, only the $PbBr_2$ on Cu interface has bonding at the interface between cations and anions, with no cation-cation or anion-anion bond. This intuition is confirmed as interface calculations show the $PbBr_2$ on Cu interface to have the lowest interface energy by more than 20 eV over the nearest interface energy. The interface energy is calculated by

$$E_{intf} = \frac{1}{2A}\left(E_{rel}^{intf} - E_{rel}^{slab}(t_1) - E_{rel}^{slab}(t_2)\right), \quad (18)$$

where A is the surface area, the first energy term is the ground state energy of the relaxed interface, and the second and third terms are the ground state energy of each relaxed surface that comprises the interface. The interface energy for each system begins to converge after 7 atomic layers of $CsPbBr_3$ (or 3 unit cells of each material) and are shown in fig 16.

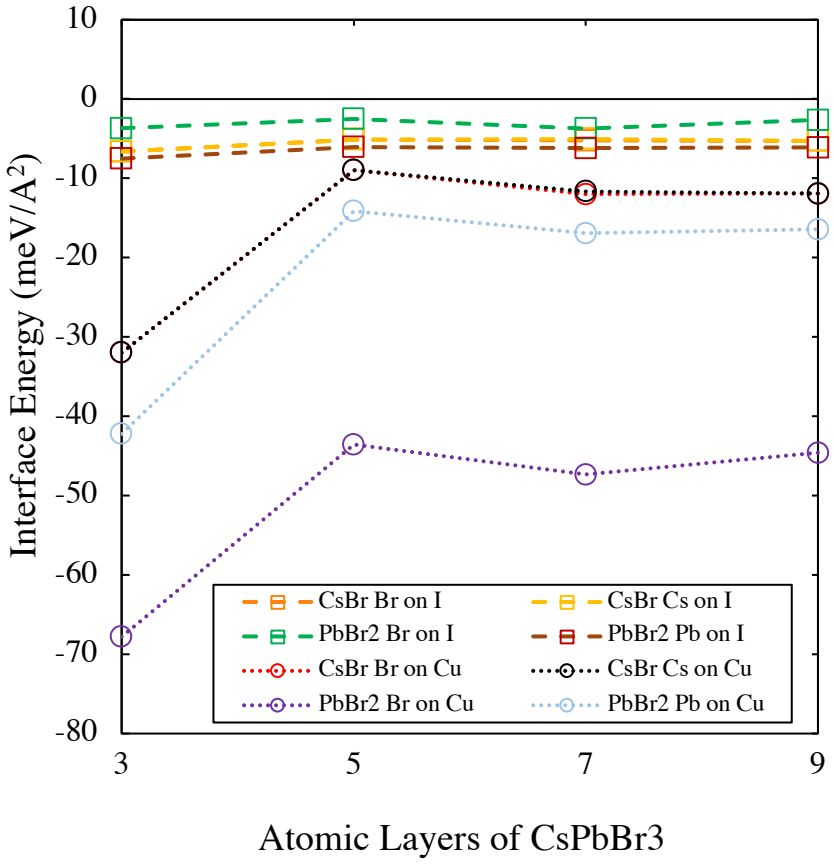

Figure 16. Interface energy for all 8 interfaces between $CsPbBr_3$ and CuI as a function of the number of atomic layers of $CsPbBr_3$. The x-axis could also be seen as the number of unit cells of each material from 1-4 cells i.e. 3 atomic layers = 1 unit cell, 5 layers = 2 unit cells, etc.

The charge density of the interface between a surface and vacuum is different than that of the interface between two different materials. This can be visualized from the difference between the charge density of the two materials interfaced with vacuum and the interface formed between the two materials given by $\Delta\rho = \rho_{intf} - \rho_{CsPbBr_3} - \rho_{CuI}$. Figure 17 shows the charge density difference for each interface visualized using VESTA; the charge density regions of accumulation and depletion are represented by colored isosurfaces. Stability of an interface can be determined qualitatively by looking to the charge regions at the interface; alternating regions of positive and negative charge density across an interface are more stable than adjacent positive or adjacent negative charge density regions. The $PbBr_2$ on Cu interface has alternating regions of accumulation and depletion regions across the interface, solidifying it as the most likely interface to occur between these materials.

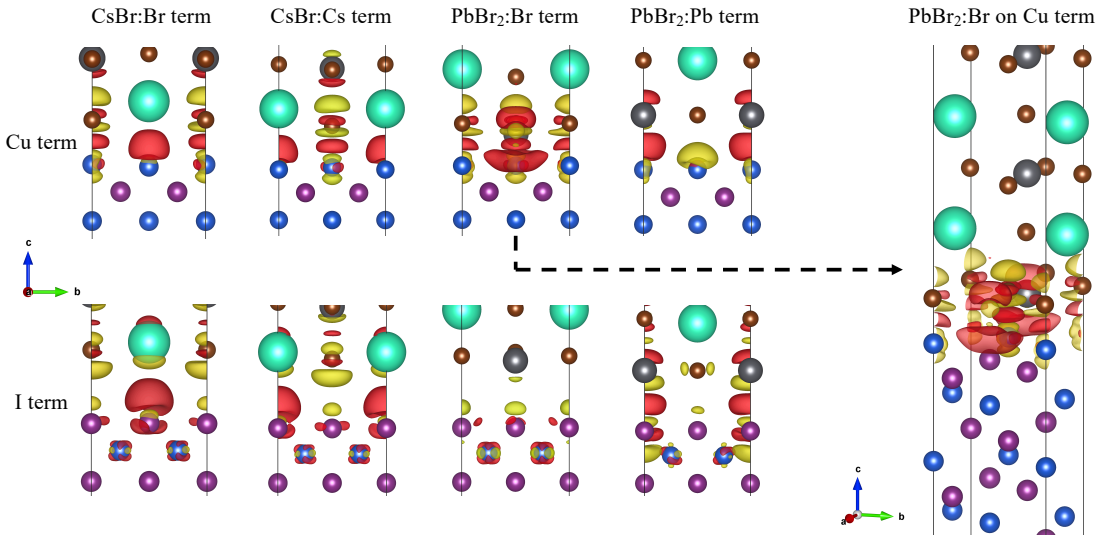

Figure 17. Charge density difference for each of the 8 interfaces between $CsPbBr_3$ and CuI viewed along the a-axis; columns are labeled by the upper surface termination while rows are labeled by the lower surface termination. Yellow isosurfaces indicate charge accumulation (positive value) while red isosurfaces indicate charge depletion (negative value). The most stable system (indicated by arrow) is enlarged and shown from standard orientation on the far right. Atom coloring is the same as from Figure 14 above. In VESTA, isosurface values of 0.003 and 0.0006 e/ $Å^3$ are used for Cu and I terminated systems, respectively.

From bulk, surface and interface calculations, band offset calculations may be done to determine if the band offset is a function of layer thickness, and how charges behave at the interface; band edge eigenvalues from bulk geometry optimization calculations are used as well as core electron differences between bulk and surface models after relaxation. VASP allows one to promote core level electrons to determine the difference in Pb (Cu) 1s states for $CsPbBr_3$ (CuI) between bulk and surface calculations; this was done for the surface study within the initial state approximation where core electron eigenvalues are recalculated after the valence states are determined from self-consistency. In surface calculations, using the optimized vacuum thickness, the vacuum potential is determined where the planar averaged local potential is constant in

the vacuum region. The potential difference due to the interface is determined from the planar average local potential difference between the interface and each material that comprises the interface, where the valence and conduction band offsets are given by $VBO = E_v + \Delta V$ and $CBO = E_c + \Delta V$. The first term in each offset is given by

$$E = \epsilon^{KS} - \left(Pb_{1s}^{bulk} - Pb_{1s}^{slab}\right) - V_{vac}, \tag{19}$$

where ϵ^{KS} is the Kohn-Sham ground state valence band or conduction band eigenvalue, the 1s states are either for Pb in $CsPbBr_3$ or Cu in CuI, and the vacuum potential is the converged value in the vacuum region from surface calculations; ΔV is the difference between the local potential difference of the interface in the center of each material. The charge density difference and local potential difference as planar averages along the strain axis between the two materials is shown in fig 18 for $PbBr_2$ on Cu, where the charge density redistribution converges within about 3 atomic layers of each material.

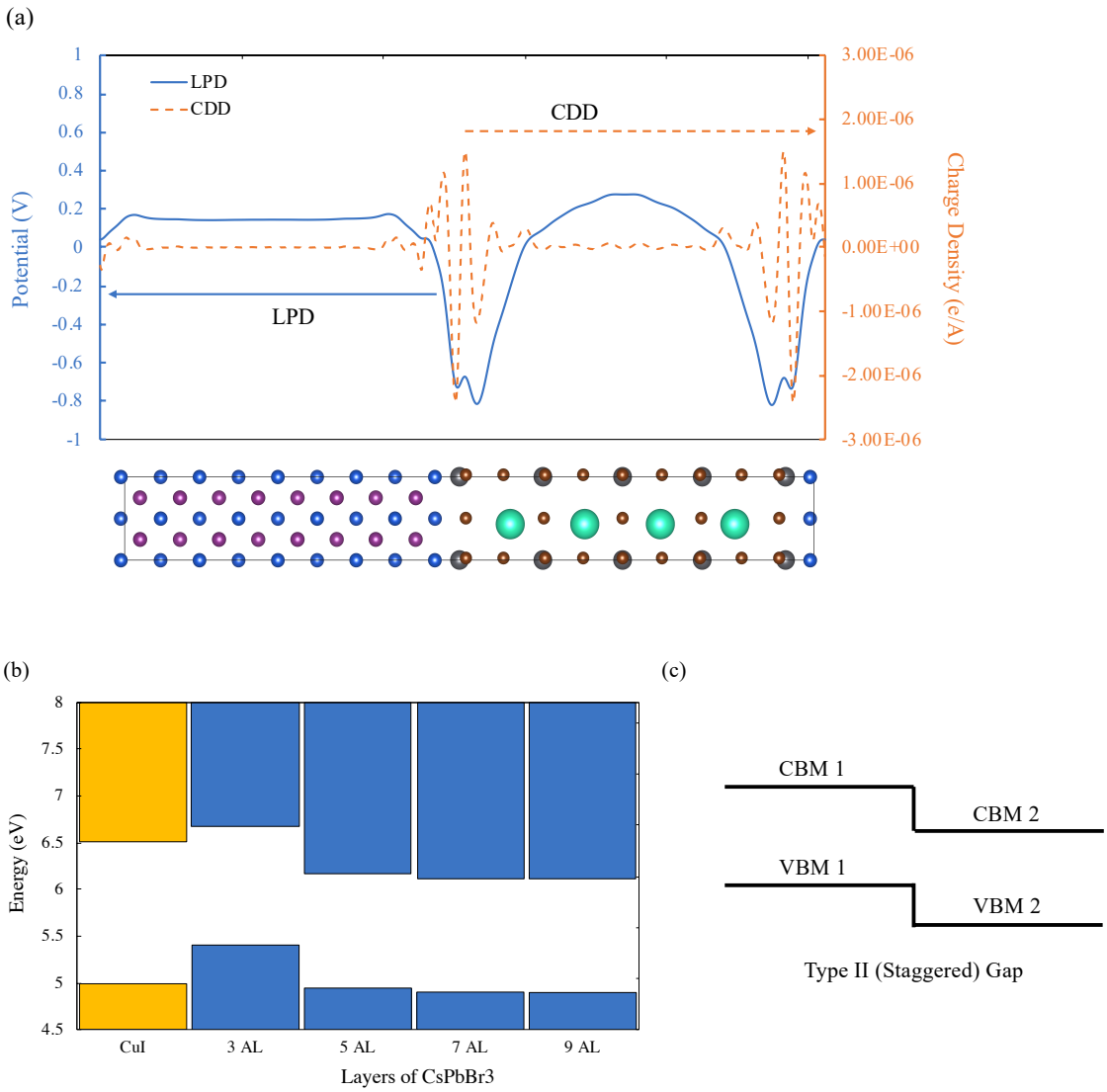

Figure 18. (a) Local potential difference and charge density difference for the 9 atomic layer $PbBr_2$ surface of $CsPbBr_3$ interfaced with the 17 atomic layer Cu surface of CuI. (b) band offset calculations, and (c) type II band offset toy-model. Arrows are included in (a) to guide the eye towards the appropriate axis.

From these calculations a type II band offset is seen between $CsPbBr_3$ and CuI, converging around 4 unit cells of each material (9 atomic layers of $CsPbBr_3$). Surface and interface calculations reveal that the $PbBr_2$ surface of $CsPbBr_3$ bonded to the Cu surface of CuI has the lowest interface energy and has cation-anion bonding across the entire interface (no similar charge repulsion), revealing a stable heterojunction. Charge

redistribution and local potential differences along the strain axis reveal bulk behavior returns within about 3 atomic layers of each material. The type II band offset seen between these two materials predicts stable charge separation at the interface, a requirement for efficient LED devices.

3.5. Summary on Polarons and Polaron Transport in HPs

Recently, a polaron manuscript was submitted for review between this manuscript's author and Los Alamos National Lab. The following is a summary of the review on polarons in halide perovskites.

Polarons are distinguished by their size and their motion through a crystal[82]. Large polarons spread across multiple atomic unit cells, distorting large portions of the local lattice around the polaron and moving coherently where scattering events are at a minimum. Small polarons are localized to a single atomic unit cell in a material and move incoherently through a lattice through phonon-assisted hopping events. Large polarons have been used to explain positive HP OE device behaviors like long charge carrier diffusion lengths, long charge carrier lifetimes, a high tolerance to defects, and ever-increasing power conversion efficiency; large polarons are thought to enhance charge carrier motion across grain boundaries[83]. Small polarons, on the other hand, have been used to describe detrimental behavior in HP OE devices like instability and degradation in ambient temperature and humidity as well as anomalous hysteresis seen in current vs voltage measurements[73,77,84–88]; hysteresis prevents accurate measurements of device parameters as forward and reverse bias sweeps of the voltage across a device result in a different current at the same voltage. Also, small polarons trap at lattice sites

creating recombination centers which reduce the power conversion efficiency in solar cells.

First principle calculations using both periodic boundary conditions[89–93] and isolated cluster[77,84,87] calculations have been used to model polarons, as was discussed in section 3.1. Distortion in the inorganic cage coupled with rotational dynamics in the organic sublattice of HPs like MAPI create an energy landscape where charges may couple to phonons in the surrounding lattice, forming self-trapped polaron states. Changing the A-site cation from MA to Cs or FA modulates the formation of small polarons, allowing for device engineering that mitigates these detrimental behaviors.

Polaronic behavior has been studied in experiments using THz spectroscopy to reveal rotational modes from A-site organic molecules coupling to photoexcited charge carriers[94]. Time-resolved optical absorption measurements were used to show long exciton lifetimes of charge carriers at the absorption band edge which is comprised of atoms in the inorganic (Pb-I) sublattice in HPs, another experimental evidence of polarons in HPs[84]. Also, the binding energy of excitons has been study through optical density measurements revealing that iodine based HPs show a reduction in energy when temperature is increased, whereas other HPs show largely temperature independent energies; iodine HPs have binding energies around 25 meV at room temperature while others have larger binding energies above 35 meV[95]. Coupling state-of-the-art DFT calculations with high-quality experiments has helped further the understanding of charge carrier photophysics in HP materials.

4. MARKET STUDY ON PEROVSKITE BASED SOLAR CELLS AND LED DEVICES

The two leading markets into which HPs most likely will first emerge will be photovoltaics (solar cells) and LEDs. Once stability and degradation issues in HP devices are resolved, scalable devices will quickly emerge into these two markets. The primary goal of HP integration will be the direct deposition onto flexible substrates, something made possible by the room temperature processing of all layers in an HP device stack (see fig 3 from the introduction). This capability will allow HPs to become a disruptive technology as it will become the most inexpensive alternative for solar cells and devices containing LEDs i.e. anything with a touch screen. To determine how disruptive HP technology may be, an understanding of the current global and US markets for solar cells and LEDs is necessary.

The current global solar market is estimated to be USD 30.8 billion (in 2016) with an expected compound annual growth rate (CAGR) of 10.9%[96]. This growth is based on current solar cell technologies i.e. silicon-based panels and is estimated to grow to USD 57.3 billion by 2022. This is obviously a very large market and HP solar cells will only tap into a small portion at first; however, this shows there is strong potential for HP solar cells to eventually corner the global solar cell market. One thing to note is how sensitive solar cell growth is to government policy. Fortunately, most of the world incentivizes the shift to renewable energies necessary to curb human-exacerbated global climate change, which will continue to allow for growth in the solar cell global market. One further barrier that currently exists is the high cost of installation for current technologies, something which will become less prevalent once HP technology is scaled[96]. The silver

lining exists, however in that even if HP panels are around the current price to install, their fabrication cost will be driven down significantly with the inclusion of HPs and will thus result in an overall decrease in the overall consumer cost of renewable, solar energy.

As the research in this manuscript was conducted in the United States, the US global market is the most likely to be the entry point for solar cells resulting from this research as well as that of the author's research group. Thus, a knowledge of the US solar cell market is prudent. The current US solar cell market is estimated to be USD 12.7 billion (in 2017) which is 22% of the global market, almost a quarter of the world's solar energy consumption[97]. Four states have shown marked increases in solar cell sales in Florida, Utah, California and Texas, where the cost to install panels has dropped nearly 70% since 2010. Installation has seen a huge CAGR of 76% in the US since the passing of the Investment Tax Credit or federal solar tax credit which allows for a 30% deduction for both personal and business installations. Industries have seen the most adoption of solar cell technologies, while growth in the residential market is slow. Even though the total US solar market has seen low growth over the last ten years, this is largely due to bad sales practices like high costs for installing and maintaining panels[97]. The total consumer costs, like in the global solar cell market, may be driven down however, by implementing HP solar cells. The US solar cell market is ready for a product like HPs which can make solar energy more cost effective to both business and private citizens. While the industrial sector in the US may be the entry point for HP technology, the long-term goal is to corner the residential market with easily installable and affordable HP solar cells.

Currently, there is a global market for perovskite solar cells within the thin-film solar cell market which is set to reach USD 5.2 billion in 2022, up from USD 3.7 billion in 2017 for a CAGR of 7%; this market is expected to increase its CAGR to 36% when perovskites move from the research to the commercial market. The US perovskite solar cell market (also research based) is expected to grow to USD 1.27 billion in 2024, up from USD 270 million in 2019; these values are estimated based on the current technology coupled with the progress of perovskite technology[98]. While estimates may tend to appear overzealous, these projections still provide hope to researchers working to stabilize HP solar cells. Once stability and degradation issues are solved, HP solar cells will quickly be scaled and enter the US consumer markets.

The current global LED market consists of numerous device-based markets growing at an overall 22% CAGR in a total market size estimated to reach USD 92.4 billion by 2022[99]. Devices range from commercial and residential lighting, to advanced chip-to-chip fiber optic interconnectivity, as well as photodiodes, where both emission and detection are possible; the later of these is where the market has grown most rapidly as touch screen devices ubiquitously implement LED photodiode technology. The universality of LEDs in modern day consumer electronics provides a robust market into which HPs may successfully emerge. While devices have seen steady decreases in cost to the consumer, there should be a larger decrease when HP LED devices come to market.

The US LED market is also robust, being valued at USD 8.05 billion in 2017, with an expect CAGR of 12.6% resulting in a value of USD 15.97 billion in 2023. One nuance about HPs is that depending on the device stack and choice of atoms in the HP,

they may also be considered OLEDs. While there is still a debate on naming conventions, organic molecules and organic polymer encapsulation have been presented as ways to improve stability and decrease degradation in HP devices (include a few citations). Therefore, it is possible for organic HPs and device stacks with organic material layers to break into the OLED market.

Finally, as the global perovskite markets are still predominantly research and development based, the true impact of perovskites on each respective market is not a simple thing to predict. However, the immense amount of positive experimental results driven by computational modeling provide hope for the future of these industries with teams achieving frequent breakthroughs[100]. Table 4 summarizes the important market values from this chapter.

Table 4. Summary of market values for global and US photovoltaic (PV), perovskite photovoltaic (PVP) and light emitting diode (LED) markets. Values in parenthesis are the year in which the future projection is expected to occur.

Market	Device	Current Value (USD Billions)	Future Value (USD Billions)	CAGR
Global	PV	30.8	57.3 (2022)	10.9
US	PV	12.7	-	-
Global	PVP	3.7	5.2 (2022)	7
US	PVP	0.27	1.27 (2022)	-
Global	LED	-	92.4 (2022)	22
US	LED	8.05	15.97 (2023)	12.6

5. CONCLUSIONS AND FUTURE RESEARCH

Due to the partial ionic bonding which occurs in HPs, polarons are expected in this class of materials. From seminal work done on hole polarons in oxide perovskite, the Hubbard corrected density functional theory method was adapted to HP materials to study the formation of hole polarons. A properly parameterized U correction value added to the ground state configuration of HPs resulted in the formation of a hole polaron as a deep-trapped state in the electronic band gap of each HP material. Geometric distortion coupled with rotational dynamics in the organic sublattice of HPs lead to the trapping of small polarons, something which is mitigated through the mixing of cations and anions. Small polaron formation is strongly dependent on the level of distortion in the inorganic framework of HP materials.

When relativistic effects are included to account for heavy atoms like Pb and I, degeneracy breaking in the energy at the band edges results in the direct electronic band gap shifting to an indirect band gap, indicating momentum dependent photoexcitation. The existence of Rashba splitting after SOC corrections were included in the DFT calculations predicted the observation of bulk photovoltaic effects in devices, specifically the circular photogalvanic effect. Inversion symmetry breaking was measured by experimental colleagues using time-resolved THz spectroscopy to reveal polarization dependent photocurrents and photoinduced polarons due to lattice distortions, confirming the theoretical calculations. Discrepancies in inversion symmetry breaking between different reports in the literature are attributed to the existence of polarons.

SOC effects and Rashba splitting were then studied in mixed HPs to show the trends in electronic properties to predict device applications. The benchmark perovskite

MAPI was revealed to have the smallest splitting parameter and thus the strongest Rashba effect, indicating its potential application in ultrafast photodetectors. The other HPs were shown to have moderate Rashba splitting, and based on the materials used for contacts, may be used in numerous spin OE devices. HPs have the potential to open numerous fields to less expensive precursors for device fabrication.

Finally, the interface between the promising inorganic HP $CsPbBr_3$ and the inorganic semiconductor CuI were studied to reveal the band offset and most probable device growth parameters. A type II band offset indicates charge separation can occur at the interface between these two materials, resulting in efficient charge injection from the CuI layer into the $CsPbBr_3$ layer. CuI is thus concluded to be an efficient and less expensive alternative to current materials in use as charge transport layers in OE devices. With larger bulk physical parameters, epitaxial growth is expected to be guided by the structure parameters of CuI.

The most promising factor surrounding HP materials in OE devices is their tunability through mixing of the stoichiometric ratio of the cations and anions for each device application. HPs may be tuned to have the optimal band gap for absorbing or emitting applications, and negative device behavior may be effectively washed out if the correct ratio of constituent atoms is found for a given application. These materials may be robustly modeling using density functional theory and other first principle modeling, while their low cost, relative ease of fabrication and subsequent measurements make HPs a robust testing ground for numerous photophysical phenomena. Device stability in solar cells is rapidly improving with better encapsulation techniques, while scalability and entrance to a consumer market is less than a decade away. With the promise of lower

costs and comparable efficiency as well as the creation of devices in already existing fabrication methodologies (e.g. slot-dye coating), HPs have the opportunity to be disruptive technologies in multiple OE fields.

Future research building from these results is as follows:

(1) The effects of spin orbit coupling on optical properties in mixed HPs will be studied using DFT and spectroscopic ellipsometry measurements. Density functional perturbation theory will be used to calculate the static and frequency dependent dielectric responses to compare to the measurements on the 4 pristine HPs $MAPbI_3$, $MAPbBr_3$, $MASnI_3$, and $MASnBr_3$. Other ratios of mixed metal and mixed halide HP will be calculated to predict the absorption and extinction coefficients of each material. A better understanding of the charge and spin dynamics in this material will help to predict other device applications for HPs.

(2) Two dimensional perovskites offer a new test ground for exotic photophysical phenomena. DFT studies of these structures along with interface studies between 2d HPs and linking cations/organic linkers will be at the forefront of HP research in the coming years. The hope is to achieve maximum device efficiency and a full theoretical understanding of the processes occurring in HP devices.

(3) The fine structure of the excited states in HP can be studied using analytical methodologies coupled with DFT structures to further clarify SOC effects in this class of materials.

(4) As stability in ambient conditions is still a challenge faced in the solar cell community, a better understanding of the interaction between the surface of halide perovskites and water is needed. First principle calculations of adsorption are

straightforward in VASP[101], where accurate surface and adsorption energies may be calculated. *In situ* synchrotron radiation XRD measurements first revealed the intermediate monohydrated phases of MAPI during degradation[102], which has since been studied using DFT and first principle thermodynamics simulations to show the favorable conditions under which water intercalates MAPI[103]. These systems may be studied for numerous mixed perovskites to predict possible stoichiometric ratios where the energetics for water intercalation are no longer favorable.

APPENDIX SECTION

The following text is taken from a manuscript co-authored by the author of this dissertation[73]: The bulk photovoltaic effect (BPVE) is observed in non-centrosymmetric crystals in this experiment. Unlike conventional p-n junction photovoltaic (PV) mechanisms, the BPVE does not require a built-in electric field. There are two mechanisms for the BPVE: (1) injection current and (2) shift current. The injection (sometimes called ballistic[104]) currents are associated with hot carriers (above bandgap excitation) and are caused by the asymmetric distribution of momenta. Photoexcited (non-thermalized) carriers lose their energy and descend to the bottom of the conduction band over a mean free path of hundreds of nanometres[105]. Injection currents results in the CPGE, which depend on the helicity (circular or linear polarized) of the incident light. The CPGE has been experimentally observed in quantum wells[106]. The driving force for the carriers in the shift current, on the other hand is the coherent evolution of wave functions[107]. The shift currents are responsible for the linear photogalvanic effect (LPGE), which depends on the linear polarization of the incident light[73].

On the macroscopic level, both injection (CPGE) and shift (LPGE) currents can be linked to second-order optical nonlinear effects, given by

$$J_\sigma = \beta_{\sigma\mu v} \boldsymbol{e}_\mu \boldsymbol{e}_v^* E_0^2 \qquad \text{(A1)}$$

where the subscripts refer to the Cartesian coordinates, $\beta_{\sigma\mu v}$ is the photogalvanic tensor, $\vec{\boldsymbol{e}}$ is the unit vector of light wave polarization, and E_0^2 is the light intensity. For both mechanisms, the current dynamics are expected to be on a subpicosecond time scale; thus, BPVE currents are often accompanied by free-space THz emission upon femtosecond optical excitation[108]. Moreover, hot carrier harvesting enables the generation

of an above-band gap photovoltage[109]. Therefore, solar cell devices possessing BPVEs can theoretically show a power conversion efficiency (PCE) that exceeds the Shockley–Queisser limit[110] for excitonic PV cells[111].

The BPVE was recently predicted for the polar configurations of the MAPI crystal structure[112,113]. The absence of inversion symmetry, together with SOC in the heavy Pb element, leads to Rashba splitting with a preferred spin orientation[114]. DFT calculations show that these spin textures can lead to the CPGE, where spin-momentum locking and angular momentum selection rules cause optical transitions between conduction and valence energy states to respond differently to light with right and left circular polarization[115].

Here, the generation of polarization-sensitive ultrafast photocurrents and free-space terahertz emission in unbiased MAPI at room temperature is shown. By measuring the amplitude and time-domain waveforms of the photocurrents under excitation with different optical polarizations, incidence angles, and wavelengths, the contributions of the injection photocurrents (sensitive to helicity) and shift photocurrents (sensitive to linear polarization) are extracted from the overall photocurrent response. The simultaneous observation of both “circular” and “linear” photocurrents is evidence of BPVEs in MAPI[73].

The optical scheme of the experimental setup is shown in fig A1a. For these experiments, the following experimental setup was used: a 350 nm thick MAPI film was deposited on a soda lime glass substrate with pre-patterned 120 nm thick indium tin oxide (ITO) electrodes. MAPI films were optically excited with either single-beam continuous

wave (CW) laser diodes operating at 532 nm and 650 nm or fundamental (780 nm) and second-harmonic (390 nm) radiation from femtosecond-pulsed lasers [73].

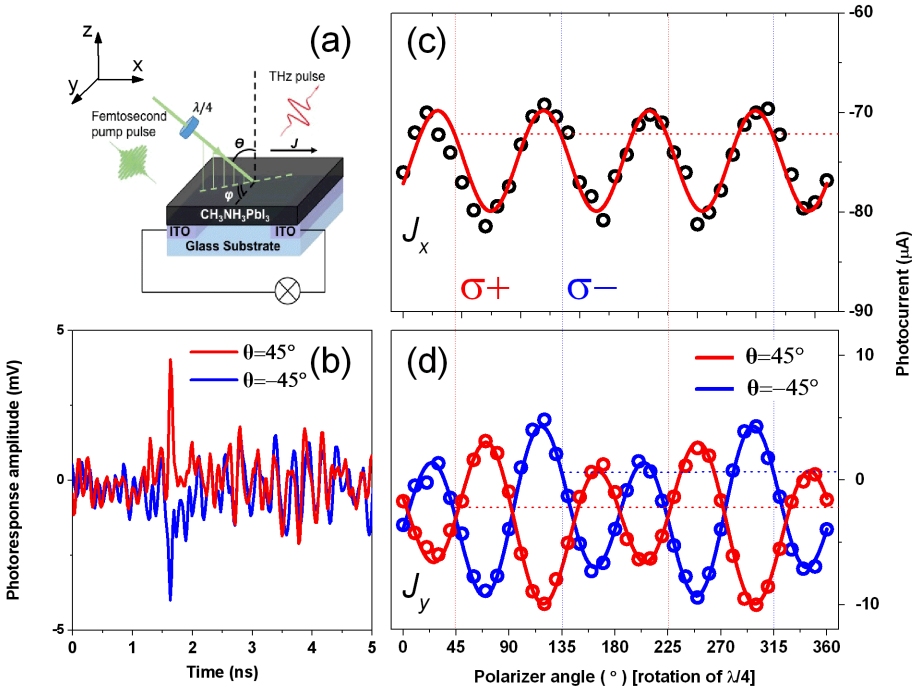

Figure A1. Polarization dependent photocurrent in unbiased MAPI sample at room temperature. Configuration (a) and temporal profiles of photocurrent response measured (b) at different incidence angles (θ=45°: red colour; θ=-45 °: blue colour) in the transversal (φ=90°)) geometry of the experiment. (c) and (d) Excitation beam polarization dependence of correspondingly longitudinal (J_x, φ=0°) and transversal (J_y, φ=90°) components of photocurrent response measured at 45° incidence. The excitation beam polarization state is controlled by rotation of the quarter wave-plate with a step of 5 degrees. 45° and 225° angles correspond to left circular polarization; 135° and 315° correspond to right circular polarization. The open circles are the experimental data. The fitting data is shown with solid lines. Reproduced with permission[73].

Photoinduced currents were measured as a voltage drop across a 50 Ω resistor in a storage oscilloscope. By changing the orientation of the sample (angle φ in fig A1a), longitudinal (J_x, when φ=0°) and transverse (J_y, when φ=90°) currents were measured with respect to the light incidence plane components of the induced photocurrent.

Polarization dependences of the induced currents were identified by measuring the amplitude of the corresponding photocurrent waveform while rotating a quarter ($\lambda/4$) waveplate positioned in front of the sample by an angle α, which varied the state of the laser polarization with a period of 90° and 180º, respectively. Figure A1b shows the waveforms of J_y components obtained at incidence angles of 45° and -45°. Figures A1c,d show the dependence of the respective photocurrents J_x and J_y excited with femtosecond pulses at 390 nm on the $\lambda/4$ waveplate angle. This shows that both J_x and J_y components of the photocurrent induced in MAPI by obliquely incident light exhibit strong polarization dependence and change their sign upon reversing the direction of incidence from 45° to -45°.

The dependence of photocurrent on the incident angle demonstrates a complex behaviour that is described by an oscillating function consisting of four components:

$$J(\alpha) = D + C \cdot \sin(2\alpha) + L1 \cdot \cos(4\alpha) + L2 \cdot \sin(4\alpha), \quad \text{(A2)}$$

where D is a polarization-independent offset ascribed to laser-heating gradients or the photo-Dember effect in the sample (we confirm the origin of this offset by sweeping the laser spot across two electrodes with a fixed polarization; see fig A5). This offset is present in all data obtained for both J_x and J_y components. To prevent the temperature gradient between the contacts necessary for the thermoelectric effect and to minimize the offset D in measurements, the laser spot was always centred between the contacts. However, owing to the finite size of the laser spot on the sample, some small polarization-independent contribution offset was always observed. The coefficient D varies from measurement to measurement because different laser sources and samples were used. The coefficient C describes the strength of the circular (helicity-dependent)

contribution to the photocurrent because the rotation of the $\lambda/4$ waveplate causes the light polarization to vary between left (σ-) and right (σ+) circular polarization with the functional form *sin(2α)*. The coefficients *L1* and *L2* in (A1) parameterize the helicity-independent photocurrents caused by the rotation of linear polarization with the functional forms *cos(4α)* and *sin(4α)*, respectively. For the α angles of 45° and 135° (purely circular polarization), the linear contribution vanishes[73].

The principal observation made from polarization-dependent measurements is that oblique incidence excitation of the MAPI sample with right and left circularly polarized light leads to the generation of transverse (J_y) photocurrents flowing along opposite directions, while the longitudinal (J_x) photocurrents depend only on the rotation of linear polarization. The amplitudes of polarization-sensitive J_x and J_y photocurrents linearly depend on the radiation intensity. Helicity dependence completely vanishes at normal incidence, while minor modulation of J_x and $\underline{J_y}$ amplitudes with a change in the linear polarization angle persists even under normally incident light (fig A6)[73].

The overall behaviour of the observed photocurrents falls under the class of second-order nonlinear effects, which include circular and linear photogalvanic effects (also known as injection and shift currents or bulk photovoltaic effect[107]) and the photon-drag effect (also known as the AC Hall effect[116] or light-induced drift currents[117]). The fundamentally distinct feature of this class of effects compared to the conventional photovoltaic optical effects, where charge carrier separation (photocurrent) is only possible when internal or external fields are applied, is the possibility to observe an intrinsic and instantaneous photocurrent response of excited carriers with no external influence on the carriers. In general, the second-order optical response is allowed in the

material if either (i) the spatial inversion symmetry of the material is broken or (ii) second-order conductivities change their sign at spatial inversion [i.e., there is a linear coupling between the current and photon wavevector (momentum)[107]]. The second case is related to the momentum transfer from a photon to the excited carrier. While both circular and linear photogalvanic effects are possible only in systems that lack inversion symmetry, the photocurrent proportional to photon momentum does not require centrosymmetry, and it is therefore allowed in any medium. Similar to the photogalvanic effect, the photon drag effect in principle occurs in response to both linearly and circularly polarized radiation. Thus, these two phenomena show an indistinguishable dependence on light polarization. However, there is a significant difference between the effects in terms of wavevectors. In particular, the photogalvanic effect is an even function of the wavevector (the photoresponse does not change sign when $\boldsymbol{k}$ is replaced with $-\boldsymbol{k}$), while photon-drag is odd (i.e., the photoresponse does change sign). Therefore, the photocurrents associated with the photogalvanic and photon-drag effects demonstrate distinct behaviour and can be distinguished in the experiment by reversing the excitation beam direction. In the experiment, the reverse of the wavevector direction can be realized by applying front and back illumination of the sample[118] (Note that there is no difference between the back and front excitations in terms of the sample geometry. As shown in fig A7, the MAPI film is covered with encapsulation glass of the same quality as the substrate). To elucidate the particular mechanisms of the polarization-sensitive photocurrents generated in the MAPI samples, the transverse component J_y is analysed under the back and front excitations. The experimental dependences of the photocurrent amplitude on the quarter-waveplate angle obtained under front and back illumination of

the MAPI sample incident at 45° with a femtosecond laser at 390 nm are summarized in fig A2[73].

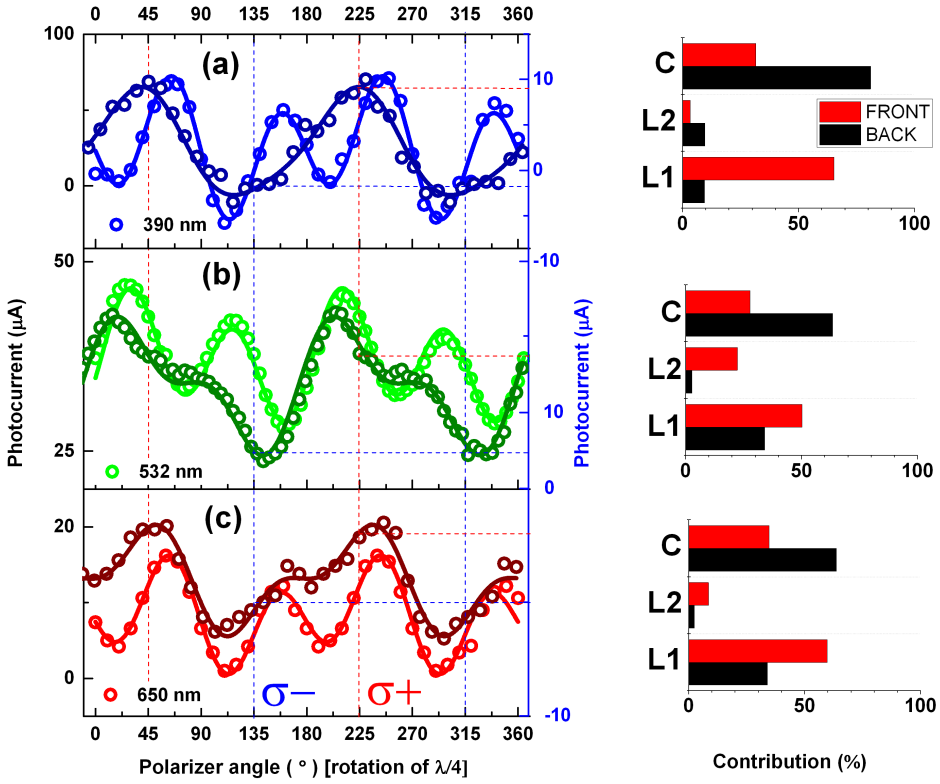

Figure A2. Wavelength dependent contributions of circular and linear polarization sensitive photocurrents. Open circles represent the experimental data obtained from the MAPI sample excited with (a) a second-harmonic femtosecond Ti:Sa laser (390 nm) and CW laser diodes operating at 532 nm (b) and 650 nm (c). The photocurrents demonstrate different behaviour when the sample is excited from the front (lighter colour) and back (darker colour) sides. The percentile contributions of different types of photocurrents extracted from fitting are shown as bar plots on the right side of the figure. Coefficients *C*, *L1*, *L2* are the fitting parameters from eq A2. Fitting is shown with solid lines. Reproduced with permission[73].

The data is fitted with eq A2, and the contributions of the different types of photocurrents is extracted from the fitting as well as being shown on a bar plot on the right side of the fig A2. Most noticeably, the photocurrents excited from the front and the

back sides of the sample show different dependence on the polarization state, while the average amplitude of the photocurrent signal remains constant. The photocurrent contribution depending on linear polarization (*L1* and *L2* coefficients in equation (A2)) decreases in the case of back excitation; by contrast, the amplitude of the circular photocurrent (*C*) is larger. To exclude any influence of the pulsed nature of the light on the amplitude and the sign of J_y photocurrents excited from the front and back sides, independent measurements were performed with a CW laser. Excitation of the sample with a CW laser leads to a DC photocurrent response, which can be detected via the occurrence of a constant positive or negative (depending on the sample orientation and incidence polarization) offset on the oscilloscope. The photocurrent traces taken with CW lasers operating at 650 nm and 532 nm under excitation from both sides of the MAPI sample are shown in fig A2. The data taken with the CW laser irradiation is in agreement with the femtosecond data and qualitatively confirm the decrease in linear *L1* and *L2* contributions and the increase in circular current *C* upon changing the direction of excitation. A decrease in the linear contribution with the change in the direction of propagation of light provides evidence for the assumption that there are two types of currents responsible for the dependence on linear polarization. Indeed, when exciting the sample from the front side, the dependence on the linear polarization is due to the combination of parallel linear photogalvanic (shift) and photon drag currents. When changing the direction of the excitation, these currents become antiparallel: the photon-drag current changes sign, while the direction of the shift current remains the same. If one assumes that the amplitudes of shift and photon-drag currents are the same, in the case of back excitation, they should compensate each other, and in turn, the linear contribution to

the photoresponse would become zero. In reality, the amplitudes and temporal dynamics of the shift and photon-drag currents are not equal and might also depend on the excitation wavelength. This qualitative picture is in agreement with the experimental data presented in fig A3, where the complete compensation of the linear component is never achieved[73].

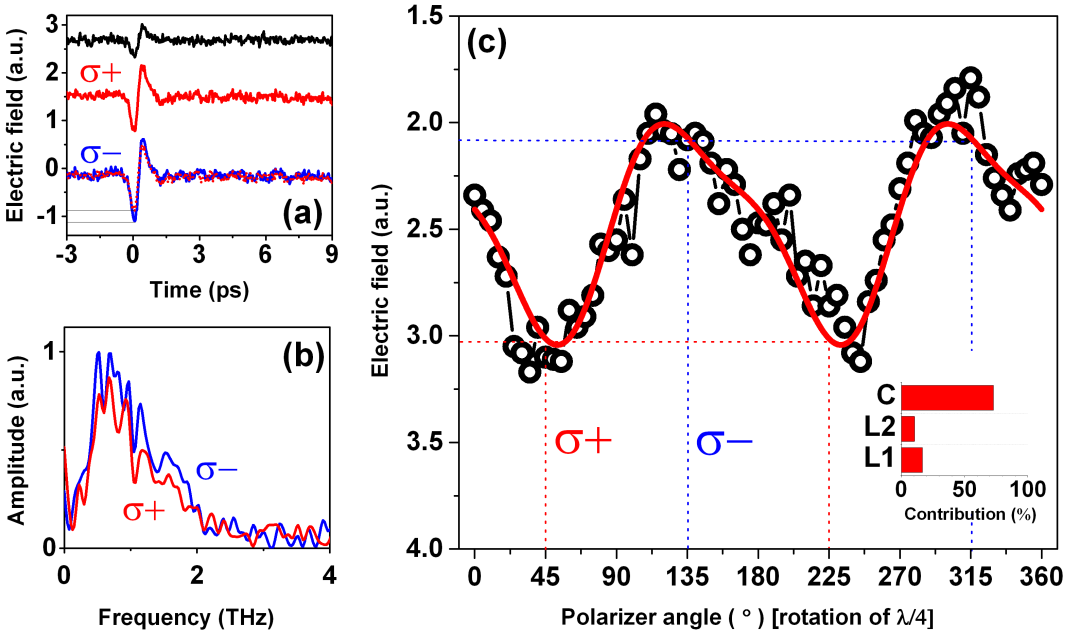

Figure A3. Polarization-dependent coherent terahertz emission from unbiased MAPI at room temperature. Excitation of the MAPI sample with femtosecond laser pulses leads to efficient emission of THz radiation. The typical transient waveforms of the emitted THz radiation detected with a GaP EO crystal at the far field under oblique excitation with linear (black curve), right circular (red curve), and left circular (blue curve) excitation beam polarization is shown in (a). Typical THz frequency spectra obtained by Fourier transform of the transient waveforms for the case of right circular (red curve) and left circular (blue curve) polarizations are shown in (b). (c) Photon-polarization dependence of the emitted THz field amplitude and fitting with equation (2) are shown with open circles and solid line correspondingly. The fitting results are shown in the bar plot on the right part of (c). Reproduced with permission[73].

Upon excitation with femtosecond pulses, the duration of the induced AC response obtained from the MAPI sample is determined by the registration system bandwidth rather than by the relaxation time of the excited carriers, while its magnitude represents the time-integrated current. Since the photocurrent is triggered by a sub-picosecond-long laser pulse and the current dynamics are also expected to be on a subpicosecond time scale, the time-varying current J can result in the emission of the THz wave in proportion to $\partial J/\partial t$. Since these photoexcitations occur in the unbiased sample, the transient photocurrents J_x and J_y or the resultant free-space emission of *p*- or *s*-polarized THz radiation, respectively, provides information regarding the internal bias near the sample surface or the relevant electrodynamics parameters. Owing to the limited time resolution in the photocurrent experiments, without information on the transient response of the current, it is difficult to conclude whether the charge current is induced directly by light illumination or indirectly by some other effects, e.g., the photo-Dember or thermo-effect. To detect the instantaneous polarization-sensitive photocurrent response upon excitation with femtosecond light pulses in the MAPI samples, time-resolved THz emission spectroscopy was used. Typical transient waveforms of the emitted THz radiation detected with electro-optic sampling at the far field under oblique excitation with linear and circular photon polarizations are shown in fig A3a. The emitted THz pulses have a subpicosecond duration and consist of a nearly single cycle oscillation. The shape of the THz waveform remains essentially constant for all incident polarizations and fluences. The THz frequency spectra obtained by Fourier transformation of the corresponding transient waveform are shown in figs A3(a) and A3(b). The frequency of the maximum THz amplitude is approximately 0.7 THz. Theoretically, the time evolution

of the shift currents differs from that of the injection and photon-drag currents[119]. The shift current directly follows the envelope of the optical pulse intensity, whereas only the onset of the other currents follows this envelope; these currents then decay with the momentum scattering time (relaxation time). However, in practice, due to the very fast momentum scattering of the carriers, the current dynamics are expected to be the same on a time scale of several hundred fs, which is in agreement with the virtually identical THz time-domain waveforms obtained under excitation with linear and circular polarization (see fig A3a)[73].

To additionally confirm that the emitted THz radiation arises from the same mechanism as the photocurrents presented in fig A2, we varied the polarization of the pump (second-harmonic) beam using a quarter-waveplate. In fig A3(c), the y-component of the generated THz electric field is plotted as a function of the polarization state of the incident pump light. The measured polarization dependence resembles those obtained with contact measurements and is well fitted with equation (A2). The results of fitting are shown in the inset of fig A3c[73].

Since the optical measurements were performed with the same film that is used for the PV cells at room temperature, it is believe that the findings can also help to understand the photophysics of perovskite solar cell devices and ultimately engineer devices with record efficiencies that would challenge the Shockley-Q limit. First, from observation of the CPGE, we conclude that MAPI films at room temperature lack inversion symmetry. There could be several reasons why this is the case. For instance, it is possible that the sample surface is supplying the necessary symmetry breaking (which would be consistent with the small response for normal incidence). Indeed, the geometry

of the sample (see fig A7) where the top and the bottom surfaces of the MAPI film are inequivalent may lead to a net broken symmetry (even if uniform generation over the layer thickness is assumed). We also note that breaking bulk inversion symmetry in our experiments can be caused by light-induced polarons, which lead to the collective distortion of the crystal lattice[120,121]. In fact, the presence or absence of polarons in the MAPI films may explain the controversial reports on MAPI polarity[122,123].

Second, the experimental data confirms the theoretically predicted Rashba spin-splitting and indirect band gap[114], which can explain the low recombination rates and high carrier diffusion length observed for MAPI[124,125,126,127]. This mechanism was recently questioned by T. Etienne et al. who performed DFT calculations for dynamical MAPI systems and concluded that the small splitting magnitude (<10 meV) might have a marginal effect on the reduction of the carrier recombination (i.e., less than an order of magnitude)[128]. However, our DFT+U calculations (with Hubbard correction and spin-orbit coupling) of the MAPI band structure in the presence of hole polarons yield much higher splitting values of 30 meV (fig A7). It is worth noting that Rashba spin splitting is caused by the local arrangements of the atoms in the unit cell rather than by the average, long-range symmetry of the crystal[129]. A larger MAPI system needs to be considered, for example, in order to compute the polaron radius and effectively estimate the contribution of the polaron effects[73].

Finally, THz emission from MAPI films implies ultrafast photocurrents with response times comparable to the carrier thermalization times (on the order of few ps[124]). Thus, a high V_{OC} close to the bandgap and even slightly above it can be obtained for perovskite PV cells with appropriate transport layers. Moreover, as was recently noted by

Spanier et al.[111] and Tan[112], photoinduced injection and shift currents can be used to construct PV device architectures with power conversion efficiencies that surpass the Shockley-Queisser limit[73].

In conclusion, the experimental evidence for optically stimulated ultrafast currents in MAPI films confirm the computational results of Rashba splitting and inversion symmetry breaking. Measurements confirm inversion symmetry breaking of the MAPI films and an indirect bandgap due to Rashba splitting at room temperature. These results further understanding of recombination suppression and long carrier diffusion lengths in MAPI. Also, observed ultrafast injection shift currents could enable next-generation perovskite PV cells with efficiencies that break the S-Q limit. These findings open new venues for perovskite spintronics, ultrafast photodetectors, and tunable THz emitters. Supplemental information plots from this work are shown below in figures A4-A9.

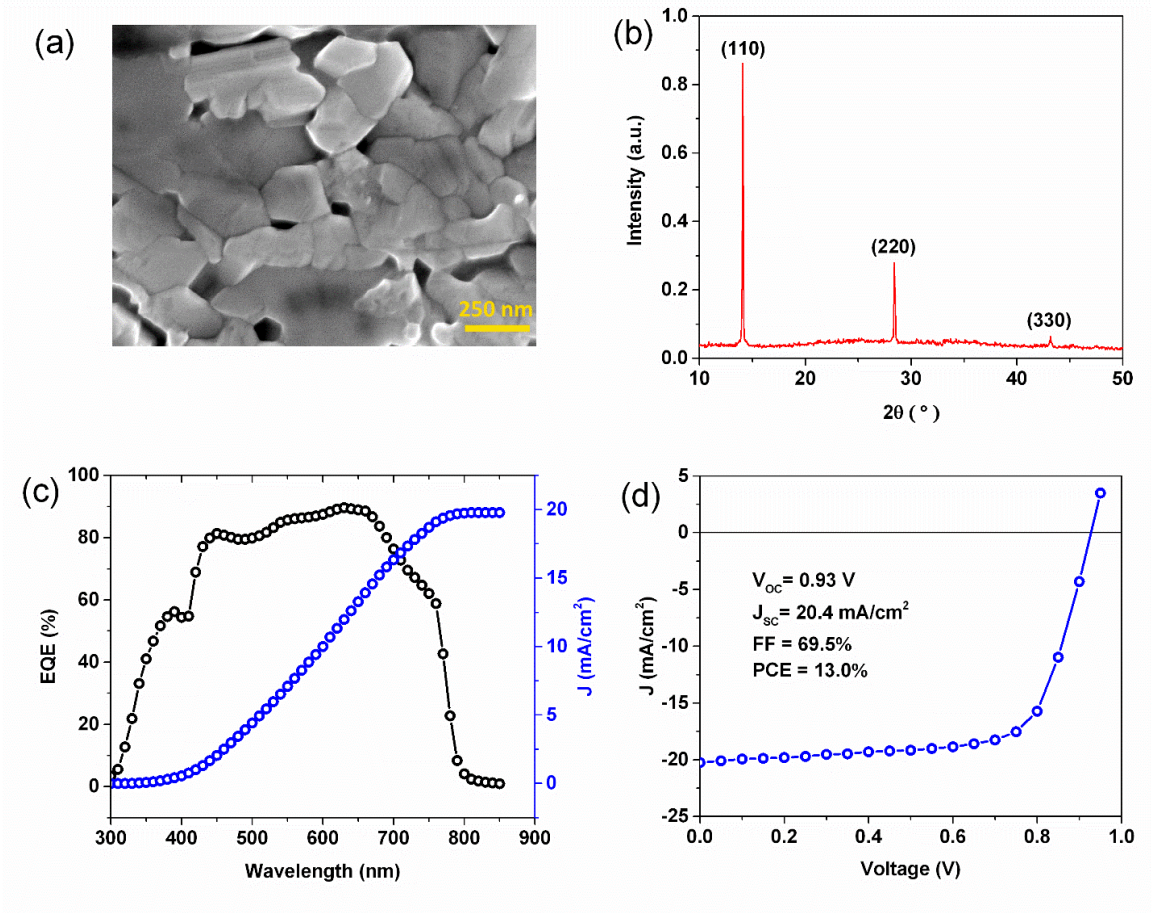

Figure A4. (a) SEM image of the $CH_3NH_3PbI_3$ film. (b) XRD pattern of the glass/$CH_3NH_3PbI_3$ sample. (c) External quantum efficiency (EQE) spectra of the PV cell device (ITO/PEDOT:PSS/$CH_3NH_3PbI_3$/C60/BCP/Ag). (d) J-V curve of the PV cell device under standard 1 sun AM1.5G 100 mW/cm^2 simulated solar irradiation. Reproduced with permission[73].

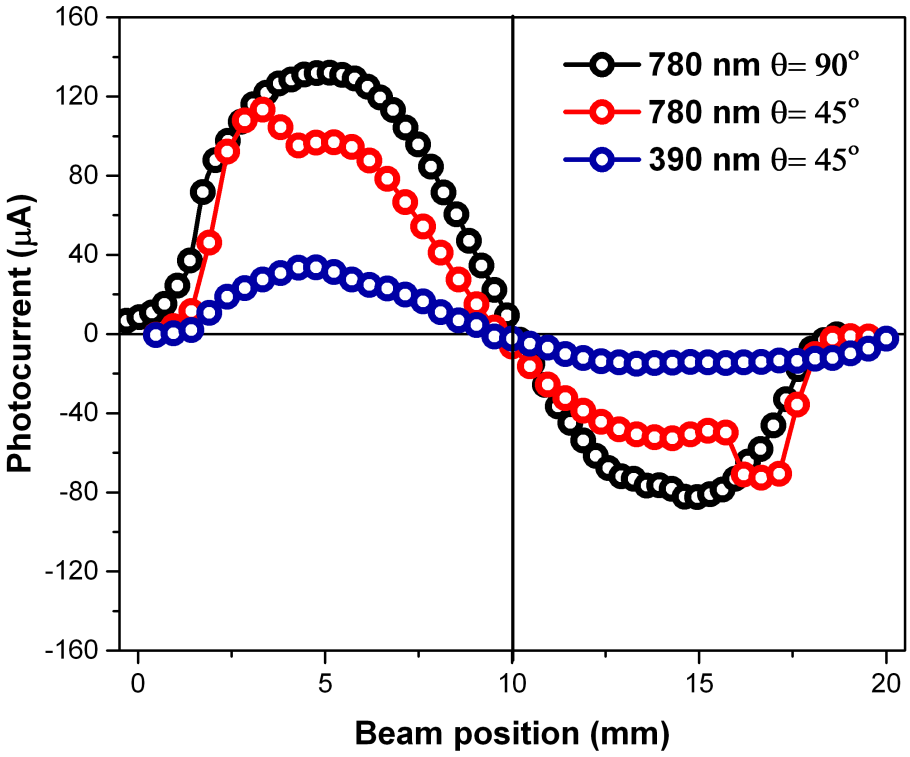

Figure A5. Polarization-insensitive photo-response dependence on the beam position measured for various excitation conditions. Reproduced with permission[73].

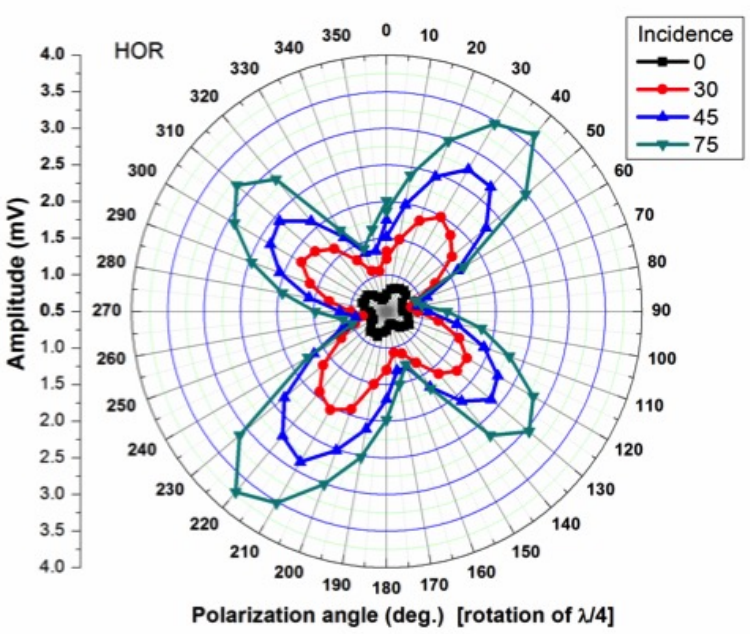

Figure A6. Polarization dependence of photocurrent in MAPI for different incidence angles. Reproduced with permission[73].

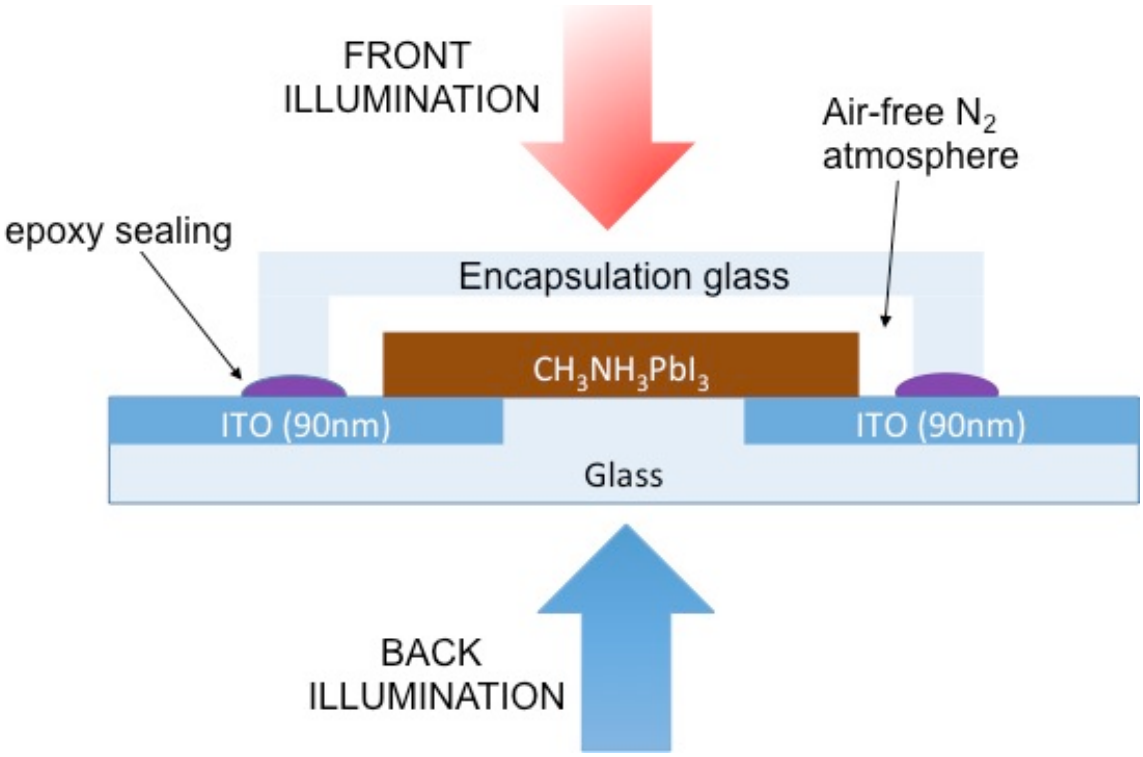

Figure A7. Model of MAPI solar cell with encapsulation showing direction of front and back illumination. Reproduced with permission[73].

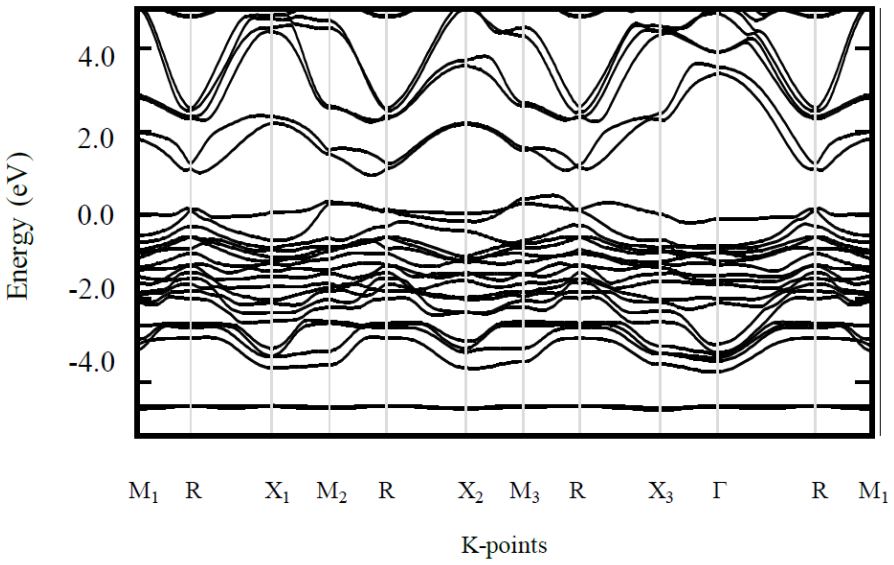

Figure A8. DFT+U band structure of MAPI using U = 8 eV on p-orbital of halide to account for self-interaction error. Spin-orbit coupling corrections result in Rashba splitting at the band gap edge (R k-point). Reproduced with permission[73].

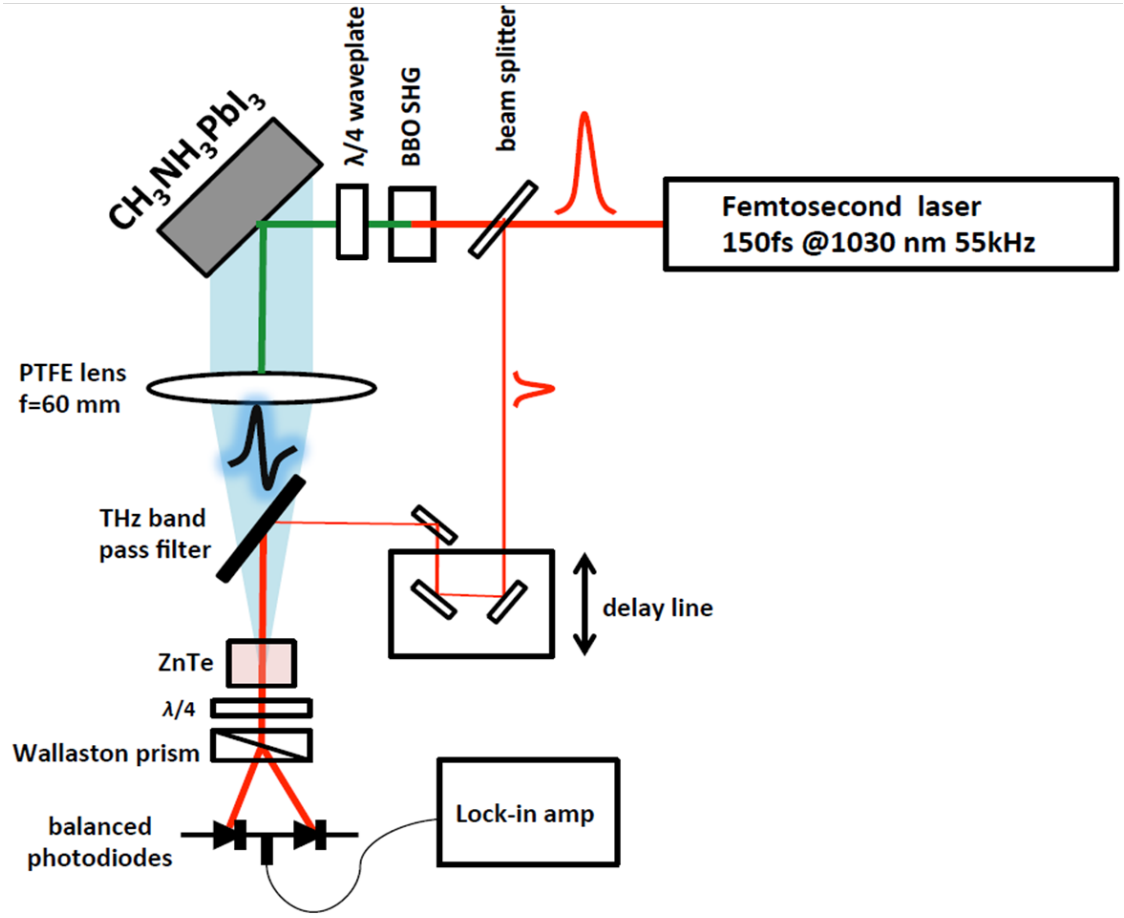

Figure A9. Principle schema of THz spectroscopy setup. Reproduced with permission[73].

REFERENCES

[1] USGS, *Mineral Commodity Summaries: Minerals Yearbook - Metals and Minerals* (2019).

[2] J.J. Yoo, S. Wieghold, M.C. Sponseller, M.R. Chua, S.N. Bertram, N.T.P. Hartono, J.S. Tresback, E.C. Hansen, J.P. Correa-Baena, V. Bulović, T. Buonassisi, S.S. Shin, and M.G. Bawendi, Energy Environ. Sci. **12**, 2192 (2019).

[3] X. Zhang, B. Xu, J. Zhang, Y. Gao, Y. Zheng, K. Wang, and X.W. Sun, Adv. Funct. Mater. **26**, 4595 (2016).

[4] Y. Wang, X. Li, J. Song, L. Xiao, H. Zeng, and H. Sun, Adv. Mater. **27**, 7101 (2015).

[5] X. Zhao, J.D.A. Ng, R.H. Friend, and Z.K. Tan, ACS Photonics **5**, 3866 (2018).

[6] Y.C. Wang, H. Li, Y.H. Hong, K. Bin Hong, F.C. Chen, C.H. Hsu, R.K. Lee, C. Conti, T.S. Kao, and T.C. Lu, ACS Nano **13**, 5421 (2019).

[7] N. Zhang, Y. Fan, K. Wang, Z. Gu, Y. Wang, L. Ge, S. Xiao, and Q. Song, Nat. Commun. **10**, 1 (2019).

[8] Y. Wang, M.L. Gao, J.L. Wu, and X.W. Zhang, Chinese Phys. B **28**, 018502 (2019).

[9] X.Y. Chin, D. Cortecchia, J. Yin, A. Bruno, and C. Soci, Nat. Commun. **6**, 1 (2015).

[10] W. Yu, F. Li, L. Yu, M.R. Niazi, Y. Zou, D. Corzo, A. Basu, C. Ma, S. Dey, M.L. Tietze, U. Buttner, X. Wang, Z. Wang, M.N. Hedhili, C. Guo, T. Wu, and A. Amassian, Nat. Commun. **9**, 1 (2018).

[11] J.W. Anthony, R.A. Bideaux, K.W. Bladh, and M.C. Nicois, *Handbook of Mineralogy. Volume III: Halides, Hydroxides, Oxides*, 1st ed. (Mineral Data Publishing, Tucson, 2001).

[12] H. Wells, J. Inorg. Chem. **3**, 195 (1893).

[13] C. Moller, Nature **182**, 1436 (1958).

[14] M. Gagliardi, *Perovskite Solar Cells: Material, Fabrication, and Global Markets* (2018).

[15] H. Kronmuller and S. Parkin, *Handbook of Magnetism and Advanced Magnetic Materials: Spintronics and Magnetoelectronics* (Johm Wiley & Sons, 2007).

[16] J.M. Frost and A. Walsh, Org. Halide Perovskite Photovoltaics From Fundam. to Device Archit. (2016).

[17] M.S. Kirschner, B.T. Diroll, P. Guo, S.M. Harvey, W. Helweh, N.C. Flanders, A. Brumberg, N.E. Watkins, A.A. Leonard, A.M. Evans, M.R. Wasielewski, W.R. Dichtel, X. Zhang, L.X. Chen, and R.D. Schaller, Nat. Commun. **10**, 1 (2019).

[18] S. Thomson, Edinburgh Instruments 1 (2018).

[19] A. Jain, S.P. Ong, G. Hautier, W. Chen, W.D. Richards, S. Dacek, S. Cholia, D. Gunter, D. Skinner, G. Ceder, and K.A. Persson, APL Mater. **1**, (2013).

[20] P. Erhart, A. Klein, D. Åberg, and B. Sadigh, Phys. Rev. B **90**, 1 (2014).

[21] F. Giustino, *Materials Modeling Using Density Functional Theory*, 1st ed. (Oxford University Press, Oxford, 2014).

[22] P. Hohenberg and W. Kohn, PRL **40**, 391 (1964).

[23] U. Von Barth and L. Hedin, J. Phys. C Solid State Phys. **5**, 1629 (1972).

[24] A. Rajagopal and J. Callaway, Phys. Rev. B **7**, 7 (1973).

[25] B.J. Alder and D.. Ceperley, Phys. Rev. Lett. **45**, 566 (1980).

[26] A. Zunger and J. P. Perdew, Phys. Rev. B **23**, 5048 (1981).

[27] E. Runge and E. Gross, Phys. Rev. Lett. **52**, 997 (1984).

[28] R. Car and M. Parrinello, Phys. Rev. Lett. **55**, 2471 (1985).

[29] S. Baroni, P. Giannozzi, and A. Testa, Phys. Rev. Lett. **58**, 1861 (1987).

[30] a. I. Lichtenstein, V.I. Anisimov, and J. Zaanen, Phys. Rev. B **52**, 5467 (1995).

[31] S.L. Dudarev, G.A. Botton, S.Y. Savrasov, C.J. Humphreys, and A.P. Sutton, Phys. Rev. B **57**, 1505 (1998).

[32] J.P. Perdew, M. Ernzerhof, and K. Burke, J. Chem. Phys. **105**, 9982 (1996).

[33] M. von Born and R. Oppenheimer, Ann. Phys. **20**, 457 (1927).

[34] J. Heyd, G.E. Scuseria, and M. Ernzerhof, J. Chem. Phys. **118**, 8207 (2003).

[35] P. Blochl, Phys. Rev. B **50**, 17953 (1994).

[36] C. Kittel, *Introduction to Solid State Physics*, 8th ed. (Johm Wiley & Sons, 2005).

[37] V.L. Gurevich and A. Thellung, Phys. Rev. B **42**, 7345 (1990).

[38] F. Birch, Phys. Rev. **71**, 809 (1947).

[39] F. Murnghan, Proc. Natl. Acad. Sci. **30**, 244 (1944).

[40] W. Press, S. Teukolsky, W. Vetterling, and B. Flannery, *Numerical Recipes: The Art of Scientific Computing*, 3rd ed. (2007).

[41] E. Pavarini, E. Koch, F. Anders, and M. Jarrell, *Modeling and Simulation From Models to Materials* (2012).

[42] P. Erhart, A. Klein, D. Åberg, and B. Sadigh, Phys. Rev. B - Condens. Matter Mater. Phys. **90**, 1 (2014).

[43] M. Radin, VASPLAB (2012).

[44] M. Gajdoš, K. Hummer, G. Kresse, J. Furthmüller, and F. Bechstedt, Phys. Rev. B - Condens. Matter Mater. Phys. **73**, 1 (2006).

[45] R. Kronig, J. Opt. Soc. Am. Rev. Sci. Instruments **12**, 547 (1926).

[46] Feynman R, Phys. Rev. **97**, 660 (1955).

[47] K. Momma and F. Izumi, J. Appl. Crystallogr. **41**, 653 (2008).

[48] L.R.V. Buizza, T.W. Crothers, Z. Wang, J.B. Patel, R.L. Milot, H.J. Snaith, M.B. Johnston, and L.M. Herz, Adv. Funct. Mater. **1**, 1 (2019).

[49] L.M. Herz, ACS Energy Lett. **2**, 1539 (2017).

[50] D. Meggiolaro, S. Motti, E. Mosconi, A. barker, J. Ball, C.A.R. Perini, F. Deschler, A. Petrozza, and F. De Angelis, Energy Environ. Sci. **11**, 702 (2018).

[51] B. Chen, M. Yang, S. Priya, and K. Zhu, J. Phys. Chem. Lett. **7**, 905 (2016).

[52] D. Li, H. Wu, H.C. Cheng, G. Wang, Y. Huang, and X. Duan, ACS Nano **10**, 6933 (2016).

[53] S. Meloni, T. Moehl, W. Tress, M. Franckevičius, M. Saliba, Y.H. Lee, P. Gao, M.K. Nazeeruddin, S.M. Zakeeruddin, U. Rothlisberger, and M. Graetzel, Nat. Commun. **7**, 10334 (2016).

[54] Y. Hou, S. Scheiner, X. Tang, N. Gasparini, M. Richter, N. Li, P. Schweizer, S. Chen, H. Chen, C.O.R. Quiroz, X. Du, G.J. Matt, A. Osvet, E. Spiecker, R.H. Fink, A. Hirsch, M. Halik, and C.J. Brabec, Adv. Mater. Interfaces **4**, 1 (2017).

[55] Y. Zhao, W. Zhou, W. Ma, S. Meng, H. Li, J. Wei, R. Fu, K. Liu, D. Yu, and Q. Zhao, ACS Energy Lett. **1**, 266 (2016).

[56] M.T. Neukom, S. Züfle, E. Knapp, M. Makha, R. Hany, and B. Ruhstaller, Sol. Energy Mater. Sol. Cells **169**, 159 (2017).

[57] S. Kim, S. Bae, S.-W. Lee, K. Cho, K.D. Lee, H. Kim, S. Park, G. Kwon, S.-W. Ahn, H.-M. Lee, Y. Kang, H.-S. Lee, and D. Kim, Sci. Rep. **7**, 1200 (2017).

[58] Y. Yuan and J. Huang, Acc. Chem. Res. **49**, 286 (2016).

[59] J. Xing, Q. Wang, Q. Dong, Y. Yuan, Y. Fang, and J. Huang, Phys. Chem. Chem. Phys. **18**, 30484 (2016).

[60] Y. Shao, Y. Fang, T. Li, Q. Wang, Q. Dong, Y. Deng, Y. Yuan, H. Wei, M. Wang, A. Gruverman, J. Shield, and J. Huang, Energy Environ. Sci. **9**, 1752 (2016).

[61] E. Welch, L. Scolfaro, and A. Zakhidov, AIP Adv. **6**, 125037 (2016).

[62] Landau, Phys. Z. Sowjetunion **3**, 664 (1933).

[63] J.T. Devreese, Phys. Today **68**, 11 (2015).

[64] T. Baikie, Y. Fang, J.M. Kadro, M. Schreyer, F. Wei, S.G. Mhaisalkar, M. Graetzel, and T.J. White, J. Mater. Chem. A **1**, 5628 (2013).

[65] A. Létoublon, S. Paofai, B. Rufflé, P. Bourges, B. Hehlen, T. Michel, C. Ecolivet, O. Durand, S. Cordier, C. Katan, and J. Even, J. Phys. Chem. Lett. **7**, 3776 (2016).

[66] T. Baikie, Y. Fang, J.M. Kadro, M. Schreyer, F. Wei, S.G. Mhaisalkar, M. Graetzel, and T.J. White, J. Mater. Chem. A **1**, 5628 (2013).

[67] P. Umari, E. Mosconi, and F. De Angelis, Sci. Rep. **4**, 4467 (2015).

[68] S. Tolba and K. Gameel, *Density Functional Theory Calculations* (IntechOpen, Reijake, 2018).

[69] J.T. Devreese, *Encyclopedia of Physics*, 3rd ed. (Wiley, 2005).

[70] M. Nagai, T. Tomioka, M. Ashida, M. Hoyano, R. Akashi, Y. Yamada, T. Aharen, and Y. Kanemitsu, Phys. Rev. Lett. **121**, 145506 (2018).

[71] C. Wolf, H. Cho, Y.H. Kim, and T.W. Lee, ChemSusChem **10**, 3705 (2017).

[72] E.I. Rashba and V.I. Sheka, Dtsch. Phys. Gesellschaft **2**, 162 (1959).

[73] P.A. Obraztsov, D. Lyashenko, P.A. Chizhov, K. Konishi, N. Nemoto, M. Kuwata-Gonokami, E. Welch, A.N. Obraztsov, and A. Zakhidov, Commun. Phys. **1**, 1 (2018).

[74] J. Wang, C. Zhang, H. Liu, R. McLaughlin, Y. Zhai, S.R. Vardeny, X. Liu, S. McGill, D. Semenov, H. Guo, R. Tsuchikawa, V. V. Deshpande, D. Sun, and Z.V. Vardeny, Nat. Commun. **10**, 1 (2019).

[75] Y.K. Jung, K.T. Butler, and A. Walsh, J. Phys. Chem. C **121**, 27351 (2017).

[76] J.S. Park, Y.K. Jung, K.T. Butler, and A. Walsh, J. Phys. Energy **1**, 016001 (2019).

[77] A.J. Neukirch, I.I. Abate, L. Zhou, W. Nie, H. Tsai, L. Pedesseau, J. Even, J.J. Crochet, A.D. Mohite, C. Katan, and S. Tretiak, J. Phys. Chem. Lett. **9**, 7130 (2018).

[78] J.B. Hoffman, A.L. Schleper, and P. V. Kamat, J. Am. Chem. Soc. **138**, 8603 (2016).

[79] Y. Rakita, S.R. Cohen, N.K. Kedem, G. Hodes, and D. Cahen, MRS Commun. **5**, 623 (2015).

[80] G. Lin, F. Zhao, Y. Zhao, D. Zhang, L. Yang, X. Xue, X. Wang, C. Qu, Q. Li, and L. Zhang, Materials (Basel). **9**, 1 (2016).

[81] R. Singh and D. Gupta, Phys. Rev. B **40**, 278 (1989).

[82] D. Emin, *Polarons*, 1st ed. (Cambridge University Press, New York, 2013).

[83] K. Miyata, T.L. Atallah, and X.Y. Zhu, Sci. Adv. **3**, 1 (2017).

[84] K. Zheng, M. Abdellah, Q. Zhu, Q. Kong, G. Jennings, C. Kurtz, M. Messing, Y. Niu, D. Gosztola, M. Al-Marri, X. Zhang, T. Pullerits, and S. Canton, J. Phys. Chem. Lett. **7**, 4535 (2016).

[85] T.M. Brenner, D.A. Egger, L. Kronik, G. Hodes, and D. Cahen, Nat. Rev. Mater. **1**, 15007 (2016).

[86] S. Kim, K.C. Ko, J.Y. Lee, and F. Illas, Phys. Chem. Chem. Phys. Phys. Chem. Chem. Phys **18**, 23755 (2016).

[87] A.J. Neukirch, W. Nie, J.C. Blancon, K. Appavoo, H. Tsai, M.Y. Sfeir, C. Katan, L. Pedesseau, J. Even, J.J. Crochet, G. Gupta, A.D. Mohite, and S. Tretiak, Nano Lett. **16**, 3809 (2016).

[88] A. Mahata, D. Meggiolaro, and F. De Angelis, J. Phys. Chem. Lett. **10**, 1790 (2019).

[89] J.M. Frost, K.T. Butler, F. Brivio, C.H. Hendon, M. Van Schilfgaarde, and A. Walsh, Nano Lett. **14**, 2584 (2014).

[90] I.O.A. Ali, D.P. Joubert, and M.S.H. Suleiman, Mater. Today Proc. **5**, 10570 (2018).

[91] J. Even, L. Pedesseau, J.M. Jancu, and C. Katan, J. Phys. Chem. Lett. **4**, 2999 (2013).

[92] M. Kepenekian, R. Robles, C. Katan, D. Sapori, L. Pedesseau, and J. Even, ACS Nano **9**, 11557 (2015).

[93] I.H. Nayyar, E.R. Batista, S. Tretiak, A. Saxena, D.L. Smith, and R.L. Martin, J. Chem. Theory Comput. **9**, 1144 (2013).

[94] E. Cinquanta, D. Meggiolaro, S.G. Motti, M. Gandini, M.J.P. Alcocer, Q.A. Akkerman, C. Vozzi, L. Manna, F. De Angelis, A. Petrozza, and S. Stagira, Phys. Rev. Lett. **122**, 166601 (2019).

[95] A.M. Soufiani, F. Huang, P. Reece, R. Sheng, A. Ho-Baillie, and M.A. Green, Appl. Phys. Lett. **107**, 1 (2015).

[96]Zion Mark. Reserach (2019).

[97] S. Cooper, Hexa Res. (2018).

[98]360 Reserach Reports (2019).

[99]LED Mark. (2017).

[100] H. Cho, S.H. Jeong, M.H. Park, Y.H. Kim, C. Wolf, C.L. Lee, J.H. Heo, A. Sadhanala, N.S. Myoung, S. Yoo, S.H. Im, R.H. Friend, and T.W. Lee, Science (80-.). **350**, 1222 (2015).

[101] VASP, (2019).

[102] J. Zhao, B. Cai, Z. Luo, Y. Dong, Y. Zhang, H. Xu, B. Hong, Y. Yang, L. Li, W. Zhang, and C. Gao, Sci. Rep. **6**, 1 (2016).

[103] Y.H. Kye, C.J. Yu, U.G. Jong, Y. Chen, and A. Walsh, J. Phys. Chem. Lett. **9**, 2196 (2018).

[104] V.I. Belinicher and B.I. Sturman, Ferroelectrics **83**, 29 (1988).

[105] B. Sturman and V. Fridkin, *The Photovoltaic and Photorefractive Effects in Noncentrosymmetric Materials* (CRC Press, 1992).

[106] M.M. Glazov and S.D. Ganichev, Phys. Rep. **535**, 101 (2014).

[107] R. von Baltz and W. Kraut, Phys. Rev. B **23**, 5590 (1981).

[108] S. Priyadarshi, M. Leidinger, K. Pierz, A.M. Racu, U. Siegner, M. Bieler, and P. Dawson, Appl. Phys. Lett. **95**, 10 (2009).

[109] S.Y. Yang, J. Seidel, S.J. Byrnes, P. Shafer, C.-H. Yang, M.D. Rossell, P. Yu, Y.-H. Chu, J.F. Scott, J.W. Ager, L.W. Martin, and R. Ramesh, Nat. Nanotechnol. **5**, 143 (2010).

[110] W. Shockley and H.J. Queisser, J. Appl. Phys. **32**, 510 (1961).

[111] J.E. Spanier, V.M. Fridkin, A.M. Rappe, A.R. Akbashev, A. Polemi, Y. Qi, S.M. Young, Z. Gu, C.J. Hawley, D. Imbrenda, G. Xiao, and C.L. Johnson, Nat. Photonics **10**, 611 (2016).

[112] L.Z. Tan, F. Zheng, S.M. Young, F. Wang, S. Liu, and A.M. Rappe, Npj Comput. Mater. **2**, 16026 (2016).

[113] J. Li and P.M. Haney, Appl. Phys. Lett. **109**, 1 (2016).

[114] F. Zheng, L.Z. Tan, S. Liu, and A.M. Rappe, Nano Lett. **15**, 7794 (2015).

[115] J. Li and P.M. Haney, Phys. Rev. B - Condens. Matter Mater. Phys. **93**, 1 (2016).

[116] P.M. Valov, A.M. Danishevskii, A.A. Kastal'skil, B.S. Ryvkin, S.M. Ryvkin, and I.D. Yaroshetskii, Sov. Phys. JETP **32**, 1038 (1971).

[117] V.M. Shalaev, C. Douketis, J.T. Stuckless, and M. Moskovits, Phys. Rev. B **53**, 11388 (1996).

[118] P. a. Obraztsov, N. Kanda, K. Konishi, M. Kuwata-Gonokami, S. V. Garnov, A.N. Obraztsov, and Y.P. Svirko, Phys. Rev. B - Condens. Matter Mater. Phys. **90**, 1 (2014).

[119] N. Laman, M. Bieler, and H.M. van Driel, J. Appl. Phys. **98**, 103507 (2005).

[120] E. Welch, L. Scolfaro, and A. Zakhidov, AIP Adv. **6**, 125037 (2016).

[121] A.J. Neukirch, W. Nie, J.-C. Blancon, K. Appavoo, H. Tsai, M.Y. Sfeir, C. Katan, L. Pedesseau, J. Even, J.J. Crochet, G. Gupta, A.D. Mohite, and S. Tretiak, Nano Lett. (2016).

[122] G. Sharada, P. Mahale, B.P. Kore, S. Mukherjee, M.S. Pavan, C. De, S. Ghara, a. Sundaresan, A. Pandey, T.N. Guru Row, and D.D. Sarma, J. Phys. Chem. Lett. **7**, 2412 (2016).

[123] Y. Kutes, L. Ye, Y. Zhou, S. Pang, B.D. Huey, and N.P. Padture, J. Phys. Chem. Lett. **5**, 3335 (2014).

[124] G. Xing, N. Mathews, S. Sun, S.S. Lim, Y.M. Lam, M. Gratzel, S. Mhaisalkar, and T.C. Sum, Science (80-.). **342**, 344 (2013).

[125] Q. Dong, Y. Fang, Y. Shao, P. Mulligan, J. Qiu, L. Cao, and J. Huang, Science **347**, 967 (2015).

[126] S.D. Stranks, G.E. Eperon, G. Grancini, C. Menelaou, M.J.P. Alcocer, T. Leijtens, L.M. Herz, A. Petrozza, and H.J. Snaith, Science **342**, 341 (2013).

[127] Y. Chen, H.T. Yi, X. Wu, R. Haroldson, Y.N. Gartstein, Y.I. Rodionov, K.S. Tikhonov, A. Zakhidov, X.-Y. Zhu, and V. Podzorov, Nat. Commun. **7**, 12253 (2016).

[128] T. Etienne, E. Mosconi, and F. De Angelis, J. Phys. Chem. Lett. **7**, 1638 (2016).

[129] X. Zhang, Q. Liu, J.-W. Luo, A.J. Freeman, and A. Zunger, Nat. Phys. **10**, 387 (2014).